# Incorporating the stable carbon isotope $^{13}$C in the ocean biogeochemical component of the Max Planck Institute Earth System Model

Bo Liu[1], Katharina D. Six[1], and Tatiana Ilyina[1]

[1]Max Planck Institute for Meteorology, Hamburg, Germany

**Correspondence:** Bo Liu (bo.liu@mpimet.mpg.de)

**Abstract.**

Direct comparison between paleo oceanic $\delta^{13}$C records and model results facilitates assessing simulated distributions and properties of water masses in the past. To accomplish this, we include a new representation of the stable carbon isotope $^{13}$C into the HAMburg Ocean Carbon Cycle model (HAMOCC), the ocean biogeochemical component of the Max Planck Institute Earth System Model (MPI-ESM). $^{13}$C is explicitly resolved for all existing oceanic carbon pools. We account for fractionation during air-sea gas exchange and for biological fractionation $\epsilon_p$ associated with photosynthetic carbon fixation during phytoplankton growth. We examine two $\epsilon_p$ parameterisations of different complexity: $\epsilon_p^{Popp}$ varies with surface dissolved $CO_2$ concentration (Popp et al., 1989), while $\epsilon_p^{Laws}$ additionally depends on local phytoplankton growth rates (Laws et al., 1995). When compared to observations of $\delta^{13}$C in dissolved inorganic carbon (DIC), both parameterisations yield similar performance. However, with regard to $\delta^{13}$C in particulate organic carbon $\epsilon_p^{Popp}$ shows a considerably improved performance than $\epsilon_p^{Laws}$, because the latter results in a too strong preference for $^{12}$C. The model also well reproduces the oceanic $^{13}$C Suess effect, i.e. the intrusion of the isotopically light anthropogenic $CO_2$ into the ocean, based on comparison to other existing $^{13}$C models and to observation-based oceanic carbon uptake estimates over the industrial period.

We further apply the approach of Eide et al. (2017a), who derived the first global oceanic $^{13}$C Suess effect estimate based on observations, to our model data that has ample spatial and temporal coverage. With this we are able to analyse in detail the underestimation of $^{13}$C Suess effect by this approach as it has been noted by Eide et al. (2017a). Based on our model we find underestimations of $^{13}$C Suess effect at 200 m by 0.24‰ in the Indian Ocean, 0.21‰ in the North Pacific, 0.26‰ in the South Pacific, 0.1‰ in the North Atlantic and 0.14‰ in the South Atlantic. We attribute the major sources of the underestimation to two assumptions in Eide et al. (2017a)'s approach: a spatially-constant preformed component of $\delta^{13}C_{DIC}$ in year 1940 and neglecting $^{13}$C Suess effect in CFC-12 free water.

## 1 Introduction

The stable carbon isotopic composition $\delta^{13}$C measured in carbonate shells of fossil foraminifera is one of the most widely used
properties in paleoceanographic research (Schmittner et al., 2017). It is defined as a normalised ratio between the stable carbon

25   isotopes $^{13}$C and $^{12}$C:

$$\delta^{13}\text{C}(\textperthousand) = \left( \frac{^{13}\text{C}/^{12}\text{C}}{R_{\text{std}}} - 1 \right) \cdot 1000, \tag{1}$$

where $R_{\text{std}}$ is an arbitrary standard ratio. In observational studies, the ratio $^{13}$C/$^{12}$C in Pee Dee Belemnite (PDB; Craig, 1957)
is conventionally used for $R_{\text{std}}$.

$\delta^{13}$C provides information on past changes of water mass distribution and properties (e.g. Curry and Oppo, 2005; Peterson

30   et al., 2014). Direct comparison between paleo $\delta^{13}$C measurements and simulated $\delta^{13}$C facilitates evaluating the ability of
Earth System Models (ESMs) to simulate paleo ocean states. For this reason, we present a new implementation of $^{13}$C in the
HAMburg Ocean Carbon Cycle model (HAMOCC6), the ocean biogeochemical component of the Max Planck Institute Earth
System Model (MPI-ESM). A comprehensive representation of $\delta^{13}$C is a timely extension of MPI-ESM in support of planned
simulations of a complete last glacial cycle within the German climate modeling initiative PalMod (Latif et al., 2016). Before

35   applying the new $^{13}$C module to paleo simulations, we evaluate it by comparison to observational data in the present day ocean.

Earlier versions of HAMOCC already featured a $^{13}$C module. HAMOCC3 included prognostic $^{13}$C variables for dissolved
inorganic carbon (DIC), particulate organic matter and calcium carbonate (Maier-Reimer, 1993). HAMOCC3 also accounted
for temperature-dependent isotopic fractionation during air-sea gas exchange (higher $\delta^{13}$C of surface DIC in colder water)
and biological fractionation during carbon fixation. Due to the simplified representation of marine biological production in

40   HAMOCC3, biological fractionation was based on fixation of inorganic carbon into non-living particulate organic matter, and
was parameterised by a spatially and temporally uniform factor. This approach for biological fractionation of $^{13}$C, however,
could not reproduce the observed large meridional gradient of $\delta^{13}$C in particulate organic matter (Goericke and Fry, 1994).
Since then, HAMOCC was refined in particular with regard to its representation of plankton dynamics, which currently re-
solves bulk phytoplankton, zooplankton, detritus, dissolved organic carbon (Six and Maier-Reimer, 1996), and nitrogen-fixing

45   cyanobacteria (Paulsen et al., 2017). We thus develop an updated $^{13}$C module that considers the refined ecosystem representa-
tion and test different non-uniform parameterisations for biological fractionation during phytoplankton growth.

We choose two parameterisations for biological fractionation that suit the complexity of our model and were successfully
applied in previous modelling studies (Hofmann et al., 2000; Schmittner et al., 2013; Tagliabue and Bopp, 2008; Jahn et al.,
2015; Dentith et al., 2020): 1) the parameterisation of Popp et al. (1989), which empirically relates biological fractionation to

50   the concentration of dissolved $CO_2$ in seawater; 2) the parameterisation of Laws et al. (1995), which considers dissolved $CO_2$
concentration and phytoplankton growth rate. We omit more complex parameterisations that include effects of cell membrane
permeability of molecular $CO_2$ diffusion, cell size, and shape (e.g. Rau et al., 1996; Keller and Morel, 1999), as HAMOCC6
does not resolve these features of plankton cells. To assess the model's performance, we run pre-industrial and present-day

simulations and compare results to observations of $\delta^{13}C$ signals in particulate organic carbon ($\delta^{13}C_{POC}$) and in dissolved
inorganic carbon ($\delta^{13}C_{DIC}$).

$\delta^{13}C_{DIC}$ measurements were mostly carried out in late 20th century and have picked up the oceanic $^{13}C$ Suess effect signal (Gruber et al., 1999). The oceanic $^{13}C$ Suess effect refers to the intrusion of anthropogenic $CO_2$ from fossil fuel combustion which carries a lower $^{13}C/^{12}C$ signal (Keeling, 1979). Recently, Eide et al. (2017a) derived an observation-based estimate of the global ocean $^{13}C$ Suess effect since pre-industrial times. Such an observation-based estimate is valuable for evaluating models at pre-industrial states (Eide et al., 2017b) and for setting up paleo simulations (O'Neill et al., 2019). Yet, Eide et al. (2017a) have noted that their approach might underestimate the oceanic $^{13}C$ Suess effect. They conjectured an underestimation of $^{13}C$ Suess effect between 0.15 - 0.24‰ at 200 m depth in 1994. However, the quantitative spatial distribution of this underestimation is unclear. Moreover, although Eide et al. (2017a) have related the underestimation to several assumptions in the approach they applied, the quantitative impact of these assumptions is still unclear as the measurements are limited in space and time to perform in-depth investigation.

Our model data includes all parameters needed to apply Eide et al. (2017a)'s procedure which relies on regressional relationships between preformed $\delta^{13}C_{DIC}$ (related to the transport of surface waters with specific DIC and DI$^{13}$C) and CFC-12 (Chlorofluorocarbon-12) partial pressure. Thus, our consistent model framework, with the complete spatio-temporal information of the hydrological and biogeochemical variables, enables us to investigate the spatial distribution of the above-mentioned potential underestimation of the oceanic $^{13}C$ Suess effect. Moreover, our model framework also allows for the attribution of the underestimation to the assumptions of the procedure Eide et al. (2017a) applied.

In the following sections, we first provide a brief introduction to the global ocean biogeochemical model HAMOCC6, followed by a description of the new $^{13}C$ module including the experimental setup (Section 2). Section 3 presents the model evaluation and Section 4 addresses our findings on the oceanic $^{13}C$ Suess effect. Summary and conclusions are given in Section 5.

## 2 Model description

### 2.1 The global ocean biogeochemical model (HAMOCC6)

HAMOCC6 (Ilyina et al., 2013; Paulsen et al., 2017; Mauritsen et al., 2019) includes biogeochemical processes in the water column and in the sediment. In the water column, the following biogeochemical tracers are simulated: dissolved inorganic carbon (DIC), total alkalinity (TA), phosphate ($PO_4$), nitrate ($NO_3$), nitrous oxide ($N_2O$), dissolved nitrogen gas ($N_2$), silicate ($SiO_4$), dissolved bioavailable iron (Fe), dissolved oxygen ($O_2$), bulk phytoplankton (Phy), cyanobacteria (Cya), zooplankton (Zoo), dissolved organic matter (DOM), particulate organic matter (POM), opal shells, calcium carbonate shells ($CaCO_3$), terrigenous material (Dust) and hydrogen sulfide ($H_2S$). The sinking speed of POM linearly increases with depth (Martin et al., 1987), whereas constant sinking speeds are set for opal, $CaCO_3$ and Dust. Except for $CaCO_3$ and opal, whose sinking speeds (30 and 25 m d$^{-1}$, respectively) are considerably faster than the horizontal velocities of ocean flow, the water-column biogeochemical tracers are transported by the hydrodynamical fields in the same manner as salinity.

The sediment module is based on Heinze et al. (1999). It simulates remineralisation and dissolution processes as in the water column concerning dissolved tracers ($PO_4$, $NO_3$, $N_2$, $O_2$, $SiO_4$, Fe, $H_2S$, DIC and TA) in the pore water and the solid sediment constituents (POM, opal, $CaCO_3$). The tracers in the pore water are exchanged with the overlying water column by diffusion.

90 Pelagic sedimentation fluxes of POM, $CaCO_3$ and opal are added to the solid components of the sediment. Below the active sediment there is one diagenetical burial layer containing only solid sediment components and representing the bedrock. To balance the loss of nutrients, TA, DIC and $SiO_4$ in the water column, constant input fluxes of DOM, $CO_3^{2-}$ and $SiO_4$ are added at the ocean surface, whose rates are derived from a linear regression of the long-term (approximately 100 years) temporal evolution of the sediment (active and burial) inventory.

95 A detailed description of HAMOCC6 is provided in Mauritsen et al. (2019) and the references therein. Different to the HAMOCC6 version in Mauritsen et al. (2019), we allow DOM degradation in low oxygen conditions until all available $O_2$ is consumed.

### 2.2 The stable carbon isotope $^{13}$C in HAMOCC6

HAMOCC6 simulates total carbon C, which is the sum of the three natural isotopes $^{12}$C, $^{13}$C and $^{14}$C. Because in nature

100 $^{12}$C constitutes about 98.9% of the total carbon and $^{13}$C only constitutes about 1.1 % (Lide, 2002), in HAMOCC we assume $^{12}$C = C. We include a $^{13}$C counterpart for each $^{12}$C prognostic variable, that is, we introduce seven new tracers for the water column and three for the sediment. $^{13}$C only mimics the $^{12}$C biogeochemical fluxes, modified by the corresponding isotopic fractionation. We assume $^{13}$C inventory to be as large as the inventory of $^{12}$C to reduce numerical errors. Consequently, the reference standard of the stable carbon isotope ratio $R_{std}$ is set to 1 in Eq. (1). In this section, we describe the implementation of

105 $^{13}$C fractionation during air-sea exchange and carbon uptake by bulk phytoplankton and by cyanobacteria. Because the isotopic fractionation during the production of calcium carbonate is small (Turner, 1982), it is not considered in this study.

#### 2.2.1 Fractionation during air-sea gas exchange

$^{13}$C isotopic fractionation during air-sea gas exchange is temperature-dependent. We adopt the calculation of $^{13}$C air-sea gas exchange recommended by the OMIP protocol (Orr et al., 2017).

110 The net air-sea $CO_2$ gas exchange flux $F$ reads

$$F = -k_{CO_2}\, \gamma_{CO_2} \left(pCO_2^{\,surf} - pCO_2^{\,atm}\right). \tag{2}$$

Here, $pCO_2^{\,surf}$ and $pCO_2^{\,atm}$ are the partial pressures of $CO_2$ in the surface seawater and in the atmosphere, respectively. The piston velocity $k_{CO_2}\,(\mathrm{ms^{-1}})$ for $CO_2$ and the solubility $\gamma_{CO_2}\,(\mathrm{mol\,L^{-1}atm^{-1}})$ of $CO_2$ are calculated following Wanninkhof (2014) and Weiss (1974), respectively.

115 The net air-sea $^{13}CO_2$ exchange flux $^{13}F$ is described similar to Eq. (2):

$$^{13}F = -\,^{13}k_{CO_2}\,^{13}\gamma_{CO_2} \left(pCO_2^{\,surf} R_g - pCO_2^{\,atm} R_{atm}\right), \tag{3}$$

in which, $R_g$ and $R_{atm}$ are the ratios of $^{13}C/^{12}C$ in surface $pCO_2$ and in atmospheric $CO_2$, respectively. Following Zhang et al. (1995), we can re-write Eq. (3) as

$$^{13}F = -k_{CO_2}\,\alpha_k\,\gamma_{CO_2}\alpha_{aq\leftarrow g}\,\left(pCO_2{}^{surf}\,\frac{R_{DIC}}{\alpha_{DIC\leftarrow g}} - pCO_2{}^{atm}\,R_{atm}\right). \tag{4}$$

120    Here, $\alpha_k = {}^{13}k_{CO_2}/k_{CO_2}$ is the kinetic fractionation factor, $\alpha_{aq\leftarrow g} = {}^{13}\gamma_{CO_2}/\gamma_{CO_2}$ is the equilibrium isotopic fractionation factor for gas dissolution (from gaseous to aqueous $CO_2$), $\alpha_{DIC\leftarrow g} = R_{DIC}/R_g$ is the equilibrium isotopic fractionation factor from gaseous $CO_2$ to DIC and $R_{DIC} = {}^{13}C_{DIC}/{}^{12}C_{DIC}$. Parameters $\alpha_k$, $\alpha_{aq\leftarrow g}$ and $\alpha_{DIC\leftarrow g}$ are obtained from laboratory experiments (Zhang et al., 1995), and are often expressed in terms of a permil fractionation factor $\epsilon(\text{‰}) = (\alpha - 1) \times 10^3$:

$$\epsilon_k = -0.81, \text{ measured at } 21°C, \tag{5}$$

125    $$\epsilon_{aq\leftarrow g} = 0.0049\,T_C - 1.31, \tag{6}$$

$$\epsilon_{DIC\leftarrow g} = 0.014\,T_C\,f_{CO_3} - 0.105\,T_C + 10.53. \tag{7}$$

Here, $T_C$ is the seawater temperature in $°C$ and $f_{CO_3} = CO_3^{2-}/DIC$ is the fraction of carbonate ions in DIC. Because in Eq. (6) the temperature dependency is weak, we use a constant $\epsilon_{aq\leftarrow g} = -1.24$, obtained at $T_C = 15°C$ in the model, following Schmittner et al. (2013). In Eq. (7) we neglect the first term $0.014\,T_C\,f_{CO_3}$, because $f_{CO_3}$ is generally smaller than 0.1 and
130    because the constant factor is one order of magnitude smaller than that of the second term $0.105\,T_C$.

### 2.2.2 Fractionation during phytoplankton growth

The lighter stable carbon isotope $^{12}C$ is preferentially utilised than $^{13}C$ during photosynthesis (O'Leary, 1988). Following Schmittner et al. (2013), we formulate this isotopic fractionation during net growth of the bulk phytoplankton and cyanobacteria as

135    $$^{13}G = R_{DIC}\,\alpha_{Phy\leftarrow DIC}\,G, \tag{8}$$

with

$$\alpha_{Phy\leftarrow DIC} = \alpha_{aq\leftarrow DIC}\,\alpha_{Phy\leftarrow aq} = \frac{\alpha_{aq\leftarrow g}}{\alpha_{DIC\leftarrow g}}\,\alpha_{Phy\leftarrow aq}. \tag{9}$$

Here $G$ ($\mu$mol C L$^{-1}$ day$^{-1}$) denotes the growth of bulk phytoplankton or cyanobacteria. $\alpha_{\text{Phy}\leftarrow\text{DIC}}$ is the isotopic fractionation factor for DIC fixation, which is determined by the equilibrium fractionation factor $\alpha_{\text{aq}\leftarrow\text{DIC}}$ from DIC to aqueous $CO_2$(aq) and by the biological fractionation factor $\epsilon_{\text{p}} = (\alpha_{\text{Phy}\leftarrow\text{aq}} - 1) \times 10^3$ related to the fixation of $CO_2$(aq). Here the subscript "Phy" denotes either the bulk phytoplankton or cyanobacteria.

We test the parameterisations for biological fractionation from Popp et al. (1989) and from Laws et al. (1995), i.e.

$$\epsilon_{\text{p}}^{\text{Popp}} = -17\log(CO_2(\text{aq})) + 3.4, \tag{10}$$

$$\epsilon_{\text{p}}^{\text{Laws}} = \left( \frac{\mu}{CO_2(\text{aq})/\rho_{\text{sea}}} - 0.371 \right)/0.015. \tag{11}$$

Here, $CO_2$(aq) ($\mu$mol L$^{-1}$) is aqueous $CO_2$ in surface water, $\mu$ (day$^{-1}$) is the specific growth rate of bulk phytoplankton or of cyanobacteria. Note that Laws et al. (1995) measured $\epsilon_{\text{aq}\leftarrow\text{Phy}}$. Because $\alpha_{\text{Phy}\leftarrow\text{aq}}$ is close to unity, $\epsilon_{\text{p}} \approx -\epsilon_{\text{aq}\leftarrow\text{Phy}}$ (Zeeb and Wolf-Gladrow, 2001). In Eq. (11), we set the seawater density $\rho_{\text{sea}}$ a constant value of $1.025$ kg L$^{-1}$. Then Eq. (11) is simplified to

$$\epsilon_{\text{p}}^{\text{Laws}} = 68.3 \frac{\mu}{CO_2(\text{aq})} - 24.7. \tag{12}$$

Both $CO_2$(aq) and $\mu$ (depending on local conditions of light, water temperature and nutrient availability) are determined in HAMOCC. Figure 1 illustrates the values of $\epsilon_{\text{p}}^{\text{Popp}}$ and $\epsilon_{\text{p}}^{\text{Laws}}$ under typical ranges of $CO_2$(aq) and $\mu$ in the ocean. When $\mu \leq 1$, $\epsilon_{\text{p}}^{\text{Laws}}$ is generally more negative than $\epsilon_{\text{p}}^{\text{Popp}}$. For high $\mu$ values, e.g. $\mu = 2$, $\epsilon_{\text{p}}^{\text{Laws}}$ is constantly less negative than $\epsilon_{\text{p}}^{\text{Popp}}$. Under high $\mu$ and low $CO_2$(aq), $\epsilon_{\text{p}}^{\text{Laws}}$ becomes positive, which is unrealistic. However, our simulated ratios of phytoplankton growth rate to dissolved $CO_2$ concentration do not produce unrealistic positive $\epsilon_{\text{p}}^{\text{Laws}}$ at any time step in this study.

## 2.3 Model set-up and experimental design

### 2.3.1 Setup

We conduct ocean-only simulations using the MPIOM-1.6.3p1 (Jungclaus et al., 2013; Notz et al., 2013; Mauritsen et al., 2019) with HAMOCC6. MPIOM is a free-surface ocean general circulation model. It uses a curvilinear grid with the grid poles located over Greenland and Antarctica. We use a low-resolution configuration with a nominal horizontal resolution of $1.5°$. This configuration has a minimum grid spacing of 15 km around Greenland and a maximum grid spacing of 185 km in the tropical Pacific. There are 40 unevenly spaced vertical levels. The layer thickness increases from 10 m in the upper ocean to 600 m in the deep ocean. The upper 100 m of the water column are represented by nine levels. The time step is 1 hour. In this set-up, we additionally include the oceanic uptake and transport of CFC-12. CFC-12 is chemically inert and can therefore be treated as a conservative and passive tracer participating in all hydro-dynamical processes within the ocean identical to e.g. salinity. The implementation of the air-sea gas exchange of CFC-12 follows the OMIP protocol (Orr et al., 2017).
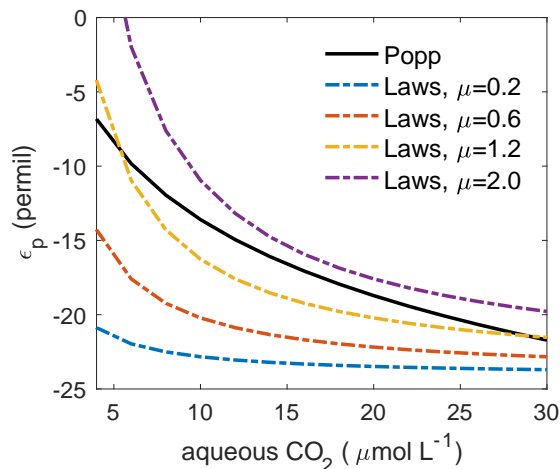
**Figure 1.** The permil biological fractionation factor $\epsilon_p$ against aqueous $CO_2$ concentration. The solid line illustrates $\epsilon_p^{Popp}$, in which the biological fractionation during phytoplankton growth is only a function of $CO_2(aq)$. The dash-dotted lines show $\epsilon_p^{Laws}$, which depends on $\mu/CO_2$, the ratio of phytoplankton growth rate to $CO_2(aq)$, for $\mu$ =0.2 (blue), 0.6 (red), 1.2 (yellow) and 2.0 (purple) day$^{-1}$.

### 2.3.2 Experimental design

We carry out pre-industrial spin-up simulations followed by historical (1850-2010) simulations. We force the model with the sea-surface boundary conditions from ERA20C (Poli et al., 2016), which covers the period 1901-2010. For the pre-industrial period, we cyclically apply the forcing of 1905-1929 and set the atmospheric $CO_2$ mixing ratio to 280 ppmv. We first conduct a

170    spin-up run without $^{13}$C tracers until the long-term averaged global net air-sea $^{13}CO_2$ flux is smaller than 0.05 Pg C yr$^{-1}$ (adequate to the C4MIP criterion for steady state conditions of <0.1 Pg C yr$^{-1}$; Jones et al., 2016). This model state is the starting point for the two spin-up runs including $^{13}$C tracers, PI_Popp and PI_Laws, which are based on the biological fractionation parametrisation $\epsilon_p^{Popp}$ (Eq. 10) and $\epsilon_p^{Laws}$ (Eq. 12), respectively.

     The $^{13}$C tracers are initialised as follows. The mean $\delta^{13}$C of the marine organic matter is about $-20\permil$ (Degens et al., 1968).

175    Therefore, we set the initial concentrations of $^{13}$C in the bulk phytoplankton, cyanobacteria, zooplankton, dissolved organic carbon, particulate organic carbon in the water column and particulate organic carbon in the sediment to 0.98 (according to Eq. 1) of their $^{12}$C counterparts. The initial $^{13}C_{DIC}$ in the water column is calculated following the relation between $\delta^{13}C_{DIC}$ and $PO_4$ (Lynch-Stieglitz et al., 1995):

$$\delta^{13}C_{DIC} = 2.7 - 1.1\,PO_4. \tag{13}$$

180    The initial concentrations of $^{13}C_{CaCO_3}$ in the water column and in the sediment, and the initial concentration of $^{13}C_{DIC}$ in pore water are set identical to their $^{12}$C counterparts.
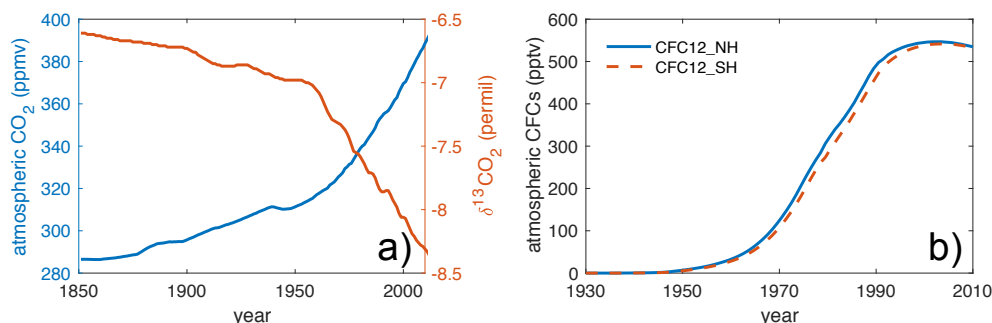
**Figure 2.** (a) The evolution of atmospheric $CO_2$ (blue, Meinshausen et al., 2017) and $\delta^{13}CO_2$ (red, Jones et al., 2016) during 1850 - 2010. (b) The evolution of atmospheric CFC-12 concentrations (Bullister, 2017). Solid blue line indicates the northern hemisphere, dashed red line indicates southern hemisphere.

The pre-industrial stable carbon isotope ratio $\delta^{13}CO_2$ of atmospheric $CO_2$ is fixed at $-6.5‰$. The input rate of dissolved organic $^{13}C$ ($DO^{13}C$) is calculated as the product of the input rate of DOC and the sea-surface $DO^{13}C$/DOC ratio; the input rate of $^{13}CO_3^{2-}$ is the product of the input rate of $CO_3^{2-}$ and the sea-surface $^{13}CO_3^{2-}/CO_3^{2-}$ ratio. This approach to determine $^{13}C$

185  input rates results in a small drift in the water-column $^{13}C$ inventory but it only has minor impact on the simulation results (see Appendix A). PI_Popp and PI_Laws are spun up for 2500 simulation years such that $^{13}C$ inventory adjusts to be consistent with the simulated biogeochemical and hydrodynamical processes. Equilibrium states are reached with 98% of the ocean volume having a drift of less than $0.001‰\,year^{-1}$ (employing the same criteria as for $^{14}C$ in OMIP protocol, Orr et al., 2017).

In the transient simulations for the historical period 1850-2010, Hist_Popp and Hist_Laws, we prescribe increasing atmo-

190  spheric $CO_2$ mixing ratios (Meinshausen et al., 2017) due to anthropogenic activities and decreasing atmospheric $\delta^{13}CO_2$ following OMIP and C4MIP protocols (Jones et al., 2016) (Fig. 2a). For the period 1850 - 1900, when forcing data is absent, we continue applying the 1905-1929 ERA20C cyclic forcing. From 1901 to 2010, we use the transient ERA20C forcing. The evolution of the atmospheric CFC-12 concentration (Fig. 2b) follows Bullister (2017). Because the atmospheric CFC-12 is slightly higher in the northern hemisphere, we prescribe a linear transition between $10°$S and $10°$N. Input rates rates of $DO^{13}C$,

195  DOC, $^{13}CO_3^{2-}$, $CO_3^{2-}$ and $SiO_4$ are kept constant, and are the same as those in the pre-industrial simulations.

## 3  Model results and observations in the late 20th century

In this section, we compare simulated $^{13}C$ between the two simulations Hist_Popp and Hist_Laws and evaluate the two experiments by comparison to observed $\delta^{13}C_{POC}$ and $\delta^{13}C_{DIC}$. The observations used here are the surface $\delta^{13}C_{POC}$ measurements assembled by Goericke and Fry (1994) and the observed $\delta^{13}C_{DIC}$, for both the surface and the interior ocean, compiled by

200  Schmittner et al. (2013). For the model-observation comparison, we first grid the observational data sets horizontally onto a 1x1 degree grid and vertically onto the 40 depth layers of the model. Multiple data points in the same grid cell in the same month and year are averaged. Then we bilinearly interpolate the simulated monthly-mean $\delta^{13}C_{POC}$ and $\delta^{13}C_{DIC}$ over a 1x1 de-

gree grid. To quantitatively compare the performance between Hist_Popp and Hist_Laws and to other $^{13}$C models, we calculate
the spatial correlation coefficient r and the normalised root mean squared error (NRMSE, normalised by the standard deviation

205 that is calculated using all the available measurements of $\delta^{13}$C$_{POC}$ or $\delta^{13}$C$_{DIC}$ during the observational periods) between model
results and observation.

## 3.1 Isotopic signature of particular organic carbon in the surface ocean

For comparison between Hist_Popp and Hist_Laws, the climatological mean state of $\delta^{13}$C$_{POC}$ is derived by averaging over
1960-1991, the period when most $\delta^{13}$C$_{POC}$ measurements were collected. In Hist_Popp, the climatological annual-mean sur-

210 face $\delta^{13}$C$_{POC}$ has a global mean value of $-22.5$‰ and it shows a distict horizontal pattern (Fig. 3a). Less negative values up
to $-19.3$‰ are found in the subtropical regions, where alkalinity is typically high and $CO_2$(aq) is consequently low. This low
$CO_2$(aq) results in a smaller isotope fractionation during carbon fixation by phytoplankton (Eq. 10, Fig. 1) with a biologi-
cal fractionation factor $\epsilon_p > -13$‰ (Fig. 3c). Poleward of the subtropical regions, $\delta^{13}$C$_{POC}$ gradually decreases. The reason
for this is twofold. First, $\epsilon_p$ decreases from $-13$ to about $-20$‰ following the increase of $CO_2$(aq). Second, the thermal ef-

215 fect of equilibrium fractionation causes about 3‰ more fractionation in the polar regions than in the tropical and subtropical
regions (according to Eqs. 7 and 9). The lowest $\delta^{13}$C$_{POC}$ of about $-30$‰ occurs close to Antarctica where highest surface
DIC concentrations are typically found because of the upwelling of deep waters and the reduced air-sea gas exchange by ice
cover (Takahashi et al., 2014). The annual range of $\delta^{13}$C$_{POC}$ (Fig. 3e), i.e. the difference between the minimum and the maxi-
mum of its climatological monthly-mean annual cycle, is low ($< 0.5$‰) in the subtropical regions and it increases polewards

220 up to $\sim 9$‰ in the Southern Ocean, mirroring meridional changes in the annual range of $CO_2$(aq).

Compared to Hist_Popp, Hist_Laws shows lower annual-mean surface $\delta^{13}$C$_{POC}$ (Fig. 3b), with a global-mean value of
$-29.9$‰ due to more negative $\epsilon_p$ (Fig. 3d). This is because $\epsilon_p^{Laws}$ (Fig. 1) is always more negative than $\epsilon_p^{Popp}$ when the simulated
mean growth rates (Figs. B1a and B1b) are lower than 1 day$^{-1}$. As $\epsilon_p^{Laws}$ increases with growth rate (Eq. 12), we find less
negative $\delta^{13}$C$_{POC}$ (up to $-24.1$‰) in the central tropical Pacific, where highest growth rates are simulated (Figs. B1a and B1b).

225 The lowest $\delta^{13}$C$_{POC}$ of $-33$‰ occurs in the Arctic Ocean and around Antarctica due to the combination of low growth rate, high
$CO_2$(aq) and low seawater temperature. The meridional range of the annual-mean $\delta^{13}$C$_{POC}$ in Hist_Laws ($\sim 9$‰) is smaller
than that of Hist_Popp ($\sim 11$‰) because for low growth rates $\epsilon_p^{Laws}$ is generally less sensitive to $CO_2$(aq) changes compared to
$\epsilon_p^{Popp}$ (Fig. 1). This also results in a smaller annual range of $\delta^{13}$C$_{POC}$ in high latitudes (Fig. 3f) than Hist_Popp (Fig. 3e). In the
low and mid latitudes, Hist_Laws show larger annual range of $\delta^{13}$C$_{POC}$ because in these regions $CO_2$(aq) concentrations are

230 relatively stable but growth rates shows noticeable seasonal variability.

Hist_Popp captures major features of the observed $\delta^{13}$C$_{POC}$ (Figs. 4a, 4c and 4e). The meridional gradient, with less negative
values in the low latitudes and minimal values around 60°S, is well reproduced. In contrast, Hist_Laws shows generally
lower $\delta^{13}$C$_{POC}$ than the observations (a global mean bias of $-8$‰) and smaller $\delta^{13}$C$_{POC}$ difference between low and high
latitudes (Figs. 4b, 4d and 4f). This is also seen in a recent study by Dentith et al. (2020), who tested $\epsilon_p^{Popp}$ and $\epsilon_p^{Laws}$ with

235 the FAMOUS model of intermediate complexity. The underestimation in the global mean and in the meridional gradient of
$\delta^{13}$C$_{POC}$ in Hist_Laws suggests that the parameters of the linear fit in Eq. (12) (slope and intercept) would need to be increased
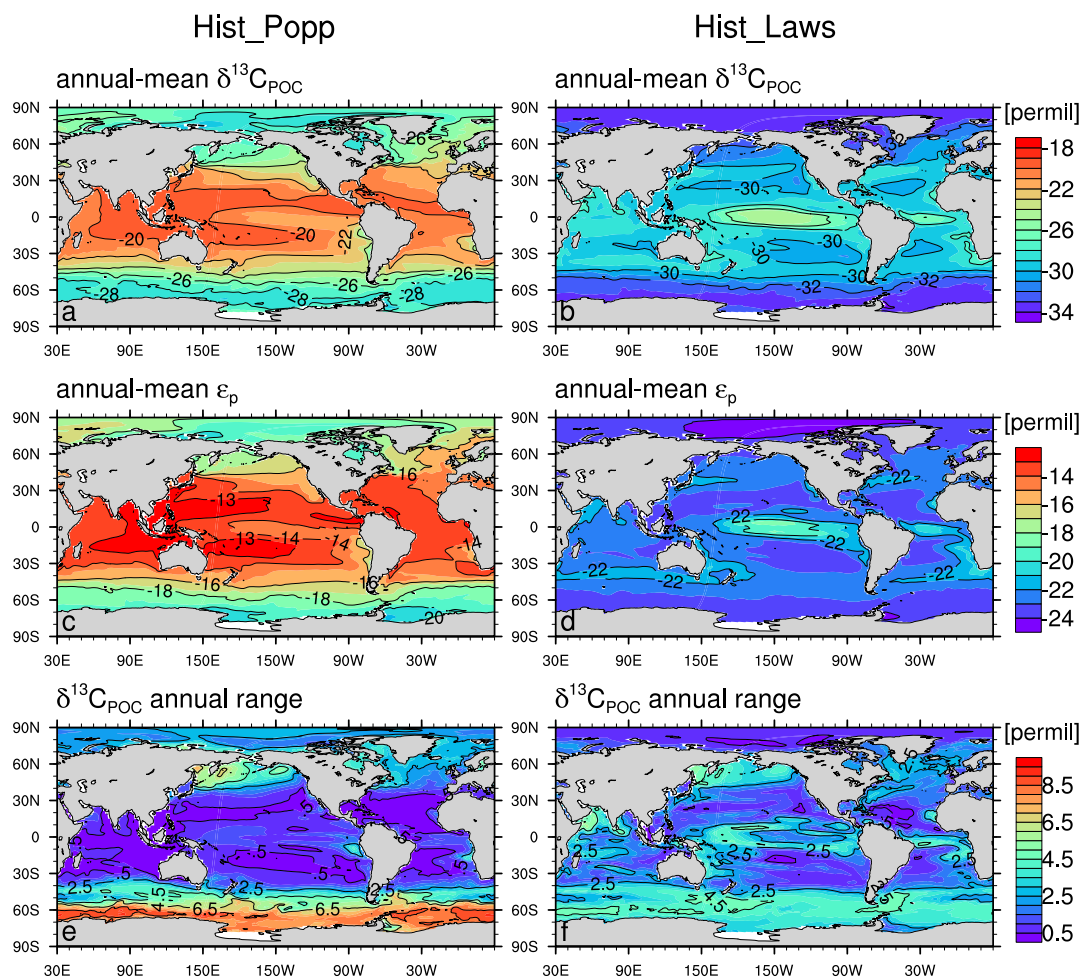
**Figure 3.** The climatological (1960-1991) annual-mean surface values for Hist_Popp (a, c, e) and Hist_Laws (b, d, f) for $\delta^{13}C_{POC}$ (a, b), $\epsilon_p$ (c, d), and for the annual range of $\delta^{13}C_{POC}$ (e, f). All values are given in permil (‰).

to gain a better performance. Around 60° S of the Atlantic Ocean (Fig. 4b), Hist_Laws simulates a smaller range of $\delta^{13}C_{POC}$ than the observations. This is also a result of the small $\delta^{13}C_{POC}$ annual range produced by $\epsilon_p^{Laws}$ (Fig. 3f). Between 40° S and 40° N in the Atlantic Ocean, Hist_Laws simulates $\delta^{13}C_{POC}$ peaks in the region of high growth rates south of the Equator, whereas the observed high $\delta^{13}C_{POC}$ values locate between the Equator and 20° N.

240 In the Indian Ocean around 45° S, Hist_Popp does not capture the prominent $\delta^{13}C_{POC}$ peak in the field data (Fig. 4e), although the simulated $CO_2(aq)$, the controlling factor in the parameterisation $\epsilon_p^{Popp}$ (Eq. 10), well reproduces the meridional variation of the observations (Fig. 4g). This is because although the empirical correlation between $\epsilon_p$ and $CO_2(aq)$, such as Eq. (10), holds true to the first order over large areas of the global ocean, other factors, such as growth rate, affect the local variability in $\epsilon_p$ (Popp et al., 1998; Hansman and Sessions, 2016; Tuerena et al., 2019). Hist_Laws captures the $\delta^{13}C_{POC}$

245
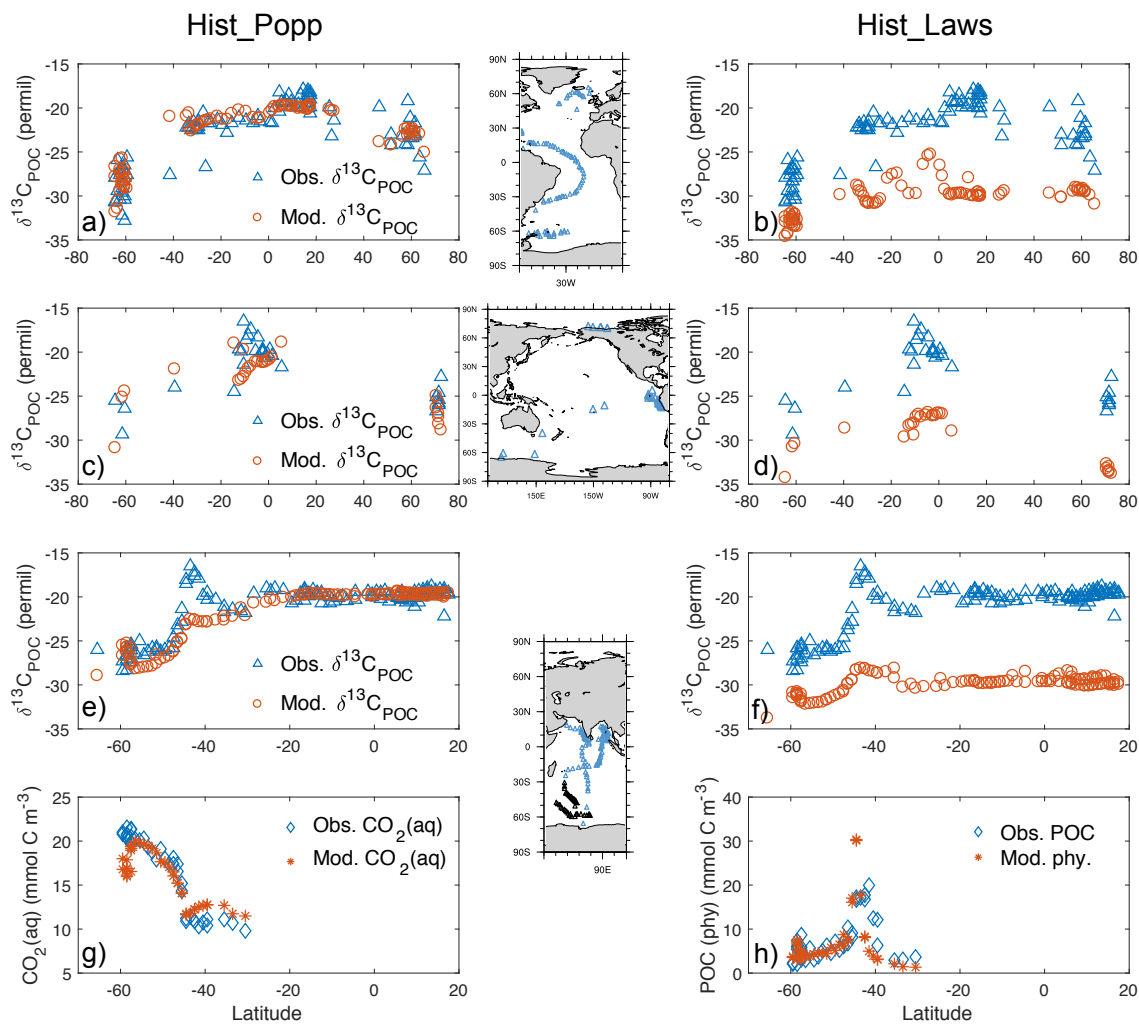
**Figure 4.** Comparison of surface $\delta^{13}C_{POC}$ (‰) observations (blue triangle) from Goericke and Fry (1994) to model data (red circle) in Hist_Popp (a, c, e) and Hist_Laws (b, d, f) for the Atlantic, Pacific and Indian Ocean, respectively. Inserted maps show cruise tracks of the measuring campaigns. (g): Comparison of simulated $CO_2$(aq) (red star) to observations (blue diamond) in the South Indian Ocean (Francois et al., 1993, measurement locations indicated by black triangles in the inset map for the Indian Ocean). (h): as panel g, but for particulate organic matter, represented by total POC in Francois et al. (1993) and by phytoplankton biomass in the model.

peak around 45° S in the observations (Fig. 4f), owing to the dependency of $\epsilon_p^{Laws}$ on phytoplankton growth rate and to the model successfully reproducing the high productivity in this region (illustrated by phytoplankton biomass, Fig. 4h). This is in alignment with the field study by Francois et al. (1993) and the model study by Hofmann et al. (2000), who ascribed this observed $\delta^{13}C_{POC}$ peak to a local high phytoplankton production during the measurement period.

250     Overall, Hist_Popp ($r = 0.84$ and NRMSE $= 0.57$) better reproduces the observed $\delta^{13}C_{POC}$ than Hist_Laws ($r = 0.71$, NRMSE $= 2.5$). Here a higher NRMSE indicates the model captures a smaller fraction of the variation in observations. The performance of Hist_Popp regarding $\delta^{13}C_{POC}$ compares well to that of the FAMOUS model (Dentith et al., 2020; Figure 8) and the UVic Earth System Model of intermediate complexity (with $r = 0.74$ and NRMSE $= 0.92$; Schmittner et al., 2013). Note that Schmittner et al. (2013) compared climatological annual-mean model output to the $\delta^{13}C_{POC}$ measurements from Goericke

255  and Fry (1994), whereas our study uses model results of the corresponding month and year of the measurements. This difference leads to a better comparison of Hist_Popp to the observed $\delta^{13}C_{POC}$ in high latitudes, particularly in the South Atlantic Ocean around $60°$ S, and therefore it is one reason for the slight better performance of Hist_Popp compared to Schmittner et al. (2013), aside from the underlying differences between the two models.

### 3.2   Isotopic signature of dissolved inorganic carbon $\delta^{13}C_{DIC}$

260 Figures 5a, 5b and 6a - 6f compare the climatological annual mean of $\delta^{13}C_{DIC}$ (averaged over 1990 - 2005, when most $\delta^{13}C_{DIC}$ measurements were collected) between Hist_Popp and Hist_Laws. The two simulations exhibit very similar $\delta^{13}C_{DIC}$ patterns for both surface and interior ocean. The surface seawater DIC is enriched in $^{13}C$ due to the preferential uptake of the light isotope $^{12}C$ by phytoplankton during primary production. As particulate organic matter sinks and is remineralised at depth, the negative $\delta^{13}C_{POC}$ signal is released. Consequently, in both Hist_Popp and Hist_Laws, $\delta^{13}C_{DIC}$ at the surface is generally

265 higher than in the ocean interior. At the surface of the equatorial central Pacific, the eastern boundary upwelling systems and the Southern Ocean south of $60°S$, lower $\delta^{13}C_{DIC}$ ($< 1.6‰$) is seen due to the upward transport of the $^{13}C$ depleted water (Figs. 5a and 5b). In the interior ocean, we find higher $\delta^{13}C_{DIC}$ ($> 1‰$) in well ventilated water masses, in particular the North Atlantic Deep Water (NADW) (Figs. 6a and 6d). The lowest $\delta^{13}C_{DIC}$ values ($< -0.5‰$) occur at depth in tropical and subtropical regions (Figs. 6a - 6f), where large amount of organic matter is remineralised.

270     The global-mean surface $\delta^{13}C_{DIC}$ of the two experiments only differs marginally ($1.64‰$ for Hist_Popp and $1.7‰$ for Hist_Laws), which is expected as they are run using the same prescribed atmospheric $\delta^{13}CO_2$ (Schmittner et al., 2013). Given very similar mean surface $DI^{13}C$, the larger vertical $DI^{13}C$ gradients in Hist_Laws, established by more negative $\delta^{13}C_{POC}$ (Figs 3a and 3b), yields lower $DI^{13}C$ concentration at depth. This adjustment of $DI^{13}C$ content in the ocean interior takes place during the pre-industrial spin-up phase of the simulations via air-sea $^{13}CO_2$ exchange (Appendix A). At the

275 end of the 2500-year spin-up, the water-column $DI^{13}C$ inventory in PI_Laws is $1.1 \times 10^{12}$ kmol lower than PI_Popp, yielding a global mean $\delta^{13}C_{DIC}$ difference of $0.25‰$ (Figs. 6g - 6i). Such interior-ocean $\delta^{13}C_{DIC}$ difference caused by using different parameterisation for biological fractionation is also seen in Jahn et al. (2015) and Dentith et al. (2020). The seasonal upward transport of the lower deep-ocean $\delta^{13}C_{DIC}$ in Hist_Laws leads to lower annual-mean surface $\delta^{13}C_{DIC}$ and larger $\delta^{13}C_{DIC}$ annual range in regions of upwelling (Figs. 5c and 5d).

280     When compared to the observed $\delta^{13}C_{DIC}$, Hist_Popp ($r = 0.81$, NRMSE $= 0.7$) has a slightly better performance than Hist_Laws ($r = 0.80$, NRMSE $= 1.1$). Hist_Laws generally shows too strong vertical gradients of $\delta^{13}C_{DIC}$ and too low $\delta^{13}C_{DIC}$ values in the ocean interior, as is seen in the depth profiles of horizontally-averaged $\delta^{13}C_{DIC}$ (Fig. 7). This points to too strong preference for the isotopically light carbon simulated by $\epsilon_p^{Laws}$ as is already discussed in Section 3.1. Given the slightly better
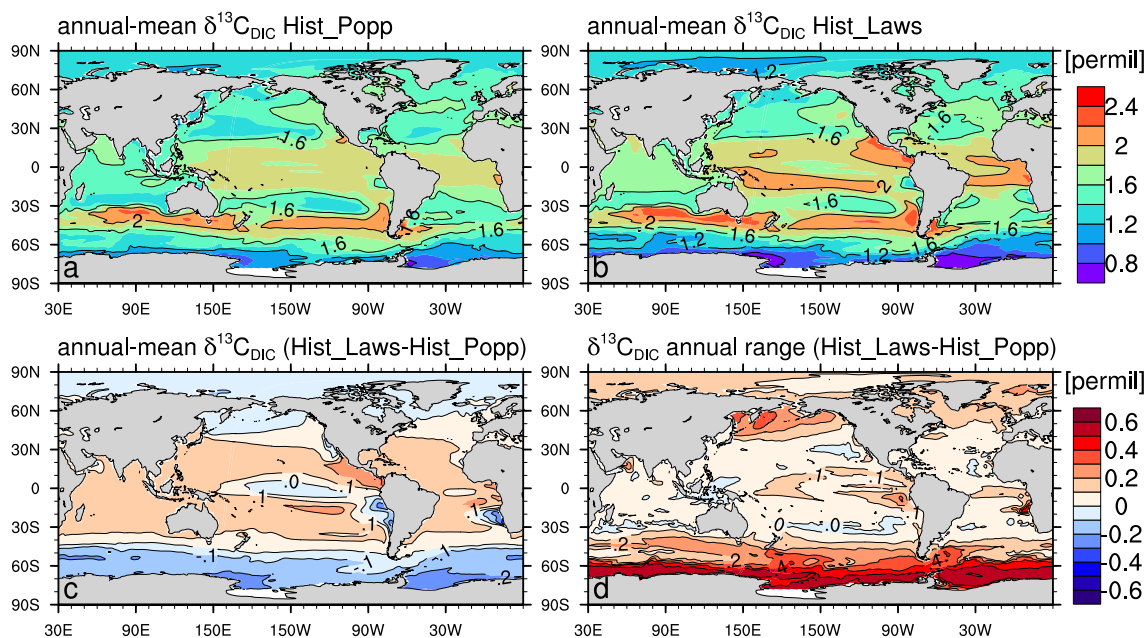
**Figure 5.** Climatological (averaged over 1990-2005) annual-mean surface $\delta^{13}C_{DIC}$ for Hist_Popp (a) and Hist_Laws (b), respectively. c and d: the difference of climatological annual-mean $\delta^{13}C_{DIC}$ between Hist_Laws and Hist_Popp, and the difference of climatological annual range of $\delta^{13}C_{DIC}$ between the two simulations, respectively.

performance of Hist_Popp than Hist_Laws regarding $\delta^{13}C_{DIC}$, we focus in the following on the comparison between Hist_Popp and observed $\delta^{13}C_{DIC}$.

Figures 8 and 9 contain model-observation comparison for the surface and interior-ocean $\delta^{13}C_{DIC}$, respectively. Overall, the magnitude and spatial distribution of the observed $\delta^{13}C_{DIC}$ is well-captured by Hist_Popp. In the surface ocean, the mean $\delta^{13}C_{DIC}$ is slightly overestimated by Hist_Popp (1.7‰ compared to 1.5‰ in observation). Positive biases are widely seen in the Indian and Pacific Ocean and the negative biases are mostly found in the Atlantic Ocean (Fig. 8c). To better understand the source of differences between model and observations, we follow the method of Broecker and Maier-Reimer (1992) to decompose $\delta^{13}C_{DIC}$ into a biological component $\delta^{13}C_{DIC}^{bio}$ and a residual component $\delta^{13}C_{DIC}^{resi}$, driven by air-sea exchange and ocean circulation:

$$\delta^{13}C_{DIC}^{bio} = \delta^{13}C_{DIC}|_{M.O.} + \frac{\Delta_{photo}}{DIC_{M.O.}} R_{C:P} (PO_4 - PO_4|_{M.O.}). \tag{14}$$

Here the subscript M.O. refers to mean ocean values, $\Delta_{photo}$ is the carbon isotope fractionation during marine photosynthesis, and $R_{C:P}$ is the C:P ratio of marine organic matter. We use $\Delta_{photo} = -19‰$ (Eide et al., 2017b) and $R_{C:P} = 122$ (Takahashi et al., 1985). To calculate $\delta^{13}C_{DIC}^{bio}$ from observations, we employ $\delta^{13}C_{DIC}|_{M.O.} = 0.5‰$, $DIC_{M.O.} = 2200\,\mu mol\,kg^{-1}$ (Eide et al., 2017b), and $PO_4$ from the World Ocean Atlas (WOA13; Garcia et al., 2013a). Considering the strong seasonality in $PO_4$
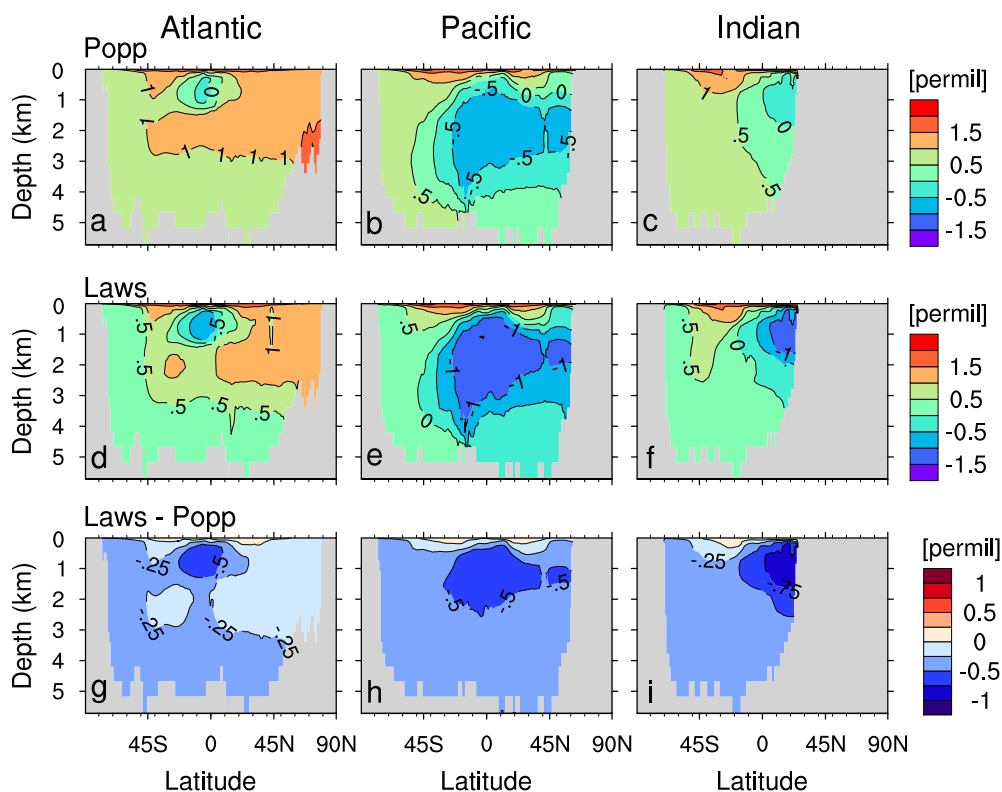
**Figure 6.** Zonal-mean $\delta^{13}C_{DIC}$ of the Atlantic Ocean (left column), the Pacific Ocean (middle column) and the Indian Ocean (right column) for Hist_Popp (a-c), Hist_Laws (d-f) and for the difference between Hist_Laws and Hist_Laws (g-i).
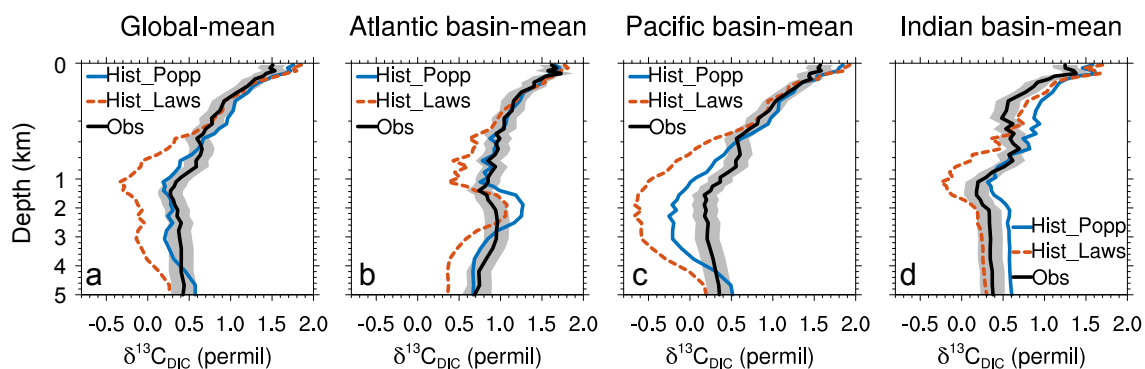
**Figure 7.** Depth profiles of horizontally-averaged $\delta^{13}C_{DIC}$ of Hist_Popp (solid blue line), Hist_Laws (dashed red line) and the observational data from Schmittner et al. (2013) (solid black line) for the global ocean (a), the Atlantic Ocean (b), the Pacific Ocean (c) and for the Indian Ocean (d). The grey shading indicates observation uncertainty of $\pm 0.15‰$, which relates to the estimated accuracy due to unresolved intercalibration issues between laboratories $(0.1 - 0.2‰$; Schmittner et al., 2013).

in the surface ocean, we select the phosphate concentration from the climatological monthly WOA data (available only for the upper 500 m of the water column) and the climatological monthly-mean model data for the same month as the $\delta^{13}C_{DIC}$

300 observations. The observed mean ocean phosphate concentration $PO_4|_{M.O.} = 1.7\,\mu mol\,kg^{-1}$ is obtained by first merging the time-mean of the $PO_4$ monthly WOA data in the upper 500 m and the $PO_4$ annual-mean WOA data below 500 m, and then mapping the combined data to the vertical grid of our model. For simulated $\delta^{13}C_{DIC}^{bio}$, the model data of $\delta^{13}C_{DIC}|_{M.O.}$, $DIC_{M.O.}$, $PO_4|_{M.O.}$ and $PO_4$ are used. The model-observation $\delta^{13}C_{DIC}^{resi}$ difference is calculated by subtracting the model-observation $\delta^{13}C_{DIC}^{bio}$ difference from the model-observation $\delta^{13}C_{DIC}$ difference.
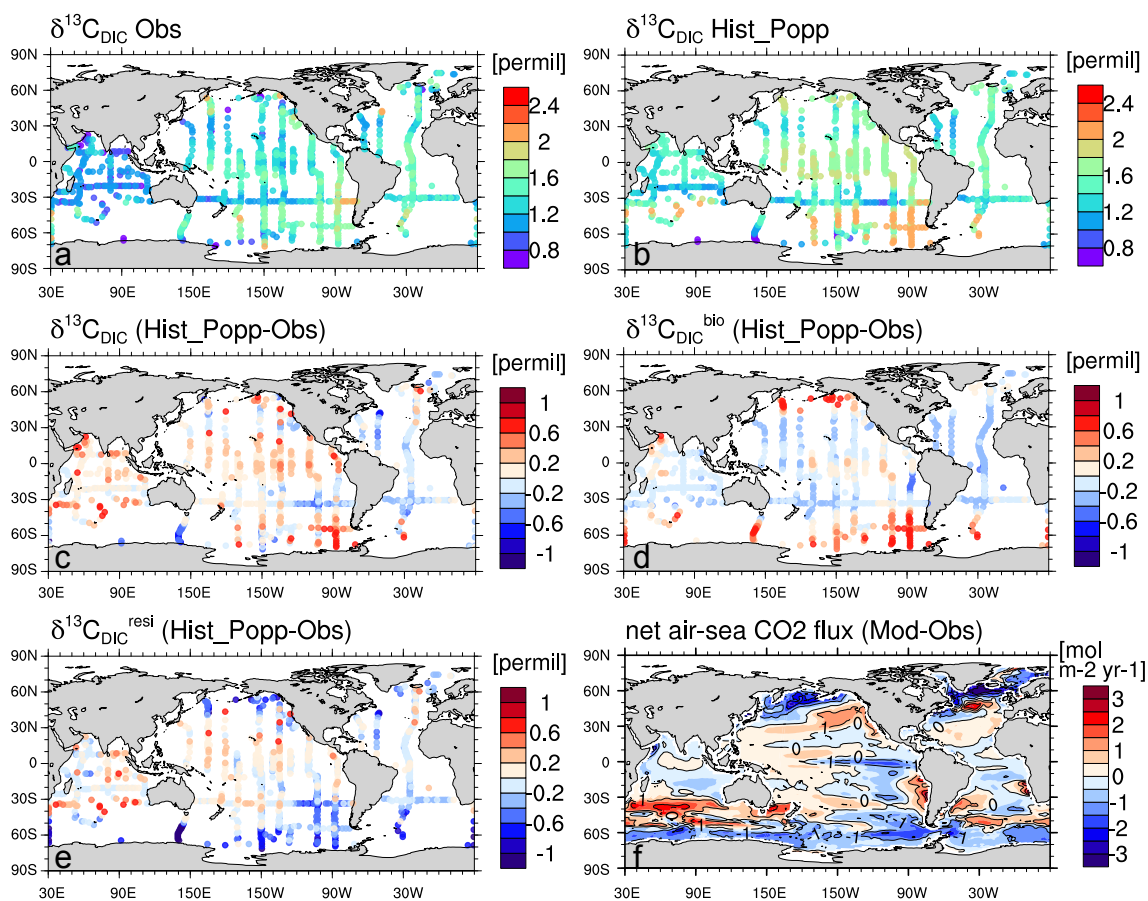
**Figure 8.** Observed surface $\delta^{13}C_{DIC}$ (Schmittner et al., 2013) (a) and simulated $\delta^{13}C_{DIC}$ in Hist_Popp sampled at the location, month and year of the observation (b). c, d, e: The difference of $\delta^{13}C_{DIC}$, its biological component $\delta^{13}C_{DIC}^{bio}$ and the residual component $\delta^{13}C_{DIC}^{resi}$ between Hist_Popp and observations. f: The net air-sea $^{13}CO_2$ flux (positive into the air, averaged over 1990-2005) difference between model and observation-based data product from Landschützer et al. (2015).

305 Between 30°N and 30 °S in the surface ocean, the simulated $\delta^{13}C_{DIC}^{bio}$ is generally lower than the observation-based $\delta^{13}C_{DIC}^{bio}$ with a mean negative bias of about $-0.1‰$ (Fig. 8d). This is caused by the underestimation of primary production in the
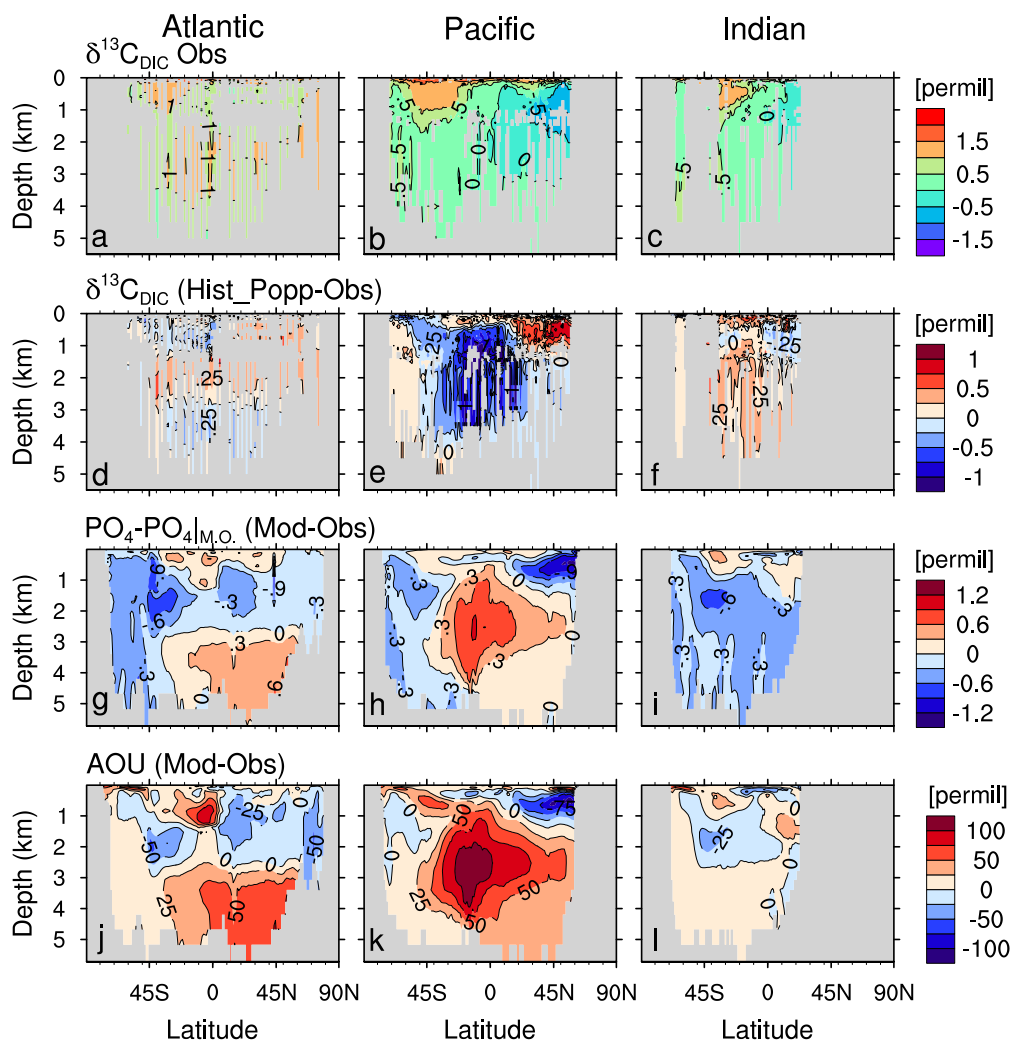
**Figure 9.** Zonal-mean distribution in the Atlantic Ocean (left column), the Pacific Ocean (middle column) and the Indian Ocean (right column) for the $\delta^{13}C_{DIC}$ observations from Schmittner et al. (2013)) (a-c), for the difference between Hist_Popp (sampled at the same location, year and month of the observations) and $\delta^{13}C_{DIC}$ measurement (d-f), for the $(PO_4 - PO_4|_{M.O.})$ difference between model and WOA data (WOA13; Garcia et al., 2013a) (g-i) and for the apparent oxygen utilisation (AOU) difference between model and WOA data (WOA13; Garcia et al., 2013b) (j-l). Here the climatological annual mean values of $PO_4$ and AOU are used for both model and WOA data because seasonal variation is negligible in the interior ocean and WOA only provides monthly data above 500 m.

subtropical gyres (due to the underestimation of phytoplankton growth rates, see Appendix B) and the consequently reduced enrichment of $^{13}C$ in surface DIC. A strong positive $\delta^{13}C_{DIC}^{bio}$ bias of 0.6 to 1‰ is seen in the North Pacific, where in the model iron is not a limiting nutrient, in contrast to observations (Moore et al., 2013). In the equatorial central Pacific, a weak positive $\delta^{13}C_{DIC}^{bio}$ bias < 0.2‰ is caused by a too high primary production. Specifically, the simulated phytoplankton growth rates in

310

this region compare well to observations, whereas the simulated phytoplankton biomass is too high (Appendix B). The latter is mainly induced by a too strong upwelling. The observed mean upward vertical velocity at $0°$, $140°$W, 60 m depth during May 1990 - June 1991 is $2.3 \times 10^{-5}$m s$^{-1}$ (Weisberg and Qiao, 2000), whereas the model simulates $3.2 \times 10^{-5}$m s$^{-1}$ for the same location and period.

315    In the Southern Ocean, a strong positive $\delta^{13}$C$_{\mathrm{DIC}}^{\mathrm{bio}}$ bias of 0.6 to 1‰ (Fig. 8d) results from a too large nutrient supply from the interior ocean to the surface. The cause for this too large nutrient supply is two fold. First, organic matter is remineralised at too shallow depths in HAMOCC, as is shown by the positive apparent oxygen utilisation (AOU) biases above 500 m south of $45°$S (Figs. 9j - 9l). Second, MPIOM simulates a too large upward transport due to too strong upwelling. In particular, below 1000 m, the simulated upward velocity shows noticeably larger magnitude ($> 5 \times 10^{-6}$ m s$^{-1}$, Fig. D1) than that of a

320    dynamically consistent and data-constrained ocean state estimate (see Figure 1 in Liang et al., 2017). Our model also features larger downward velocities than the estimate from Liang et al. (2017), which correspond to too deep mixed layer depths in the Southern Ocean (up to 3000 m, Fig. D2) than observations ($<$700 m; de Boyer Montégut et al., 2004; Holte et al., 2017).

We find strong $\delta^{13}$C$_{\mathrm{DIC}}^{\mathrm{resi}}$ negative biases of $-0.5$ to $-1‰$ (Fig. 8e) in the North Pacific and the Southern Ocean, which partially compensate the positive biases of $\delta^{13}$C$_{\mathrm{DIC}}^{\mathrm{bio}}$ (Fig. 8d) in these regions. One major cause for the negative $\delta^{13}$C$_{\mathrm{DIC}}^{\mathrm{resi}}$ bias

325    in these two regions is our model overestimating the uptake of anthropogenic carbon, as is illustrated by the net air-sea CO$_2$ difference between the model and the observation (Fig. 8f). Consequently, the decreased atmospheric $^{13}$C/$^{12}$C ratio over the industrial period further lowers $\delta^{13}$C$_{\mathrm{DIC}}$ in the two ocean regions in the model. In the Southern Ocean, a too large upward transport of $^{13}$C-depleted water at depth to the surface also contributes to a negative $\delta^{13}$C$_{\mathrm{DIC}}^{\mathrm{resi}}$ bias.

In the interior ocean, $\delta^{13}$C$_{\mathrm{DIC}}$ is controlled by remineralisation of $^{13}$C-depleted organic matter and by ocean circula-

330    tion (Broecker and Peng, 1993; Lynch-Stieglitz et al., 1995; Schmittner et al., 2013). Low $\delta^{13}$C$_{\mathrm{DIC}}$ is often found in waters of high nutrient concentration and vice versa. Thus, we find positive (negative) $\delta^{13}$C$_{\mathrm{DIC}}$ biases coincide with negative (positive) phosphate biases (Figs. 9d - 9i). In the Atlantic Ocean between 1000 and 3000m, the North Pacific above 1500 m and the Indian Ocean below 1000 m, positive $\delta^{13}$C$_{\mathrm{DIC}}$ biases and negative phosphate biases are mainly caused by a too low remineralisation, as is shown by the negative AOU biases (Figs 9j - 9l). North of $30°$S in the Atlantic Ocean, the negative $\delta^{13}$C$_{\mathrm{DIC}}$ biases below

335    3000 m, together with the negative $\delta^{13}$C$_{\mathrm{DIC}}$ biases between 1000 and 3000 m, suggest too strong $\delta^{13}$C$_{\mathrm{DIC}}$ vertical gradients in the model (Fig. 9d). This results from a too shallow lower boundary of the NADW cell, constantly located above 2800 m, compared to an estimated NADW lower boundary of about 4300 m deep at $26°$N (Msadek et al., 2013; Smeed et al., 2017). A possible reason for the shallow NADW in the model is that the Lower North Atlantic Deep Water (LNADW), forming from the Denmark Strait Overflow Water and the Iceland-Scotland Overflow Water, is not dense enough to flow further southward.

340    This is can be seen from the CFC-12 distribution along the zonal Section A5 at $24°$N (Fig. D3). The observed deeper CFC-12 maximum (3000-4500 m west of $60°$W) indicates the presence of LNADW (Dutay et al., 2002), which is not represented in our model.

We find the strongest negative $\delta^{13}$C$_{\mathrm{DIC}}$ bias in the deep eastern equatorial Pacific (Fig. 9e). The cause is the 'nutrient trapping' problem in the model, characterised by too high nutrient concentrations in the deep eastern equatorial Pacific (Fig. 9h), which

345    is a persistent problem in many ESMs (Aumont et al., 1999; Dietze and Loeptien, 2013). Based on sensitivity experiments with

the Geophysical Fluid Dynamics Laboratory model and UVic model, Dietze and Loeptien (2013) concluded the primary cause of the 'nutrient trapping' problem is likely model biases in physical ocean state, in particular, the poor representation of the Equatorial Intermediate Current System and Equatorial Deep Jets. The latter two current systems are indeed poorly represented in our model as well. Specifically, the zonal current at 1000 m depth (typical depth for the the Equatorial Intermediate Current

350  System) shows too little spatial variability and too low speeds of $\sim 0.2$ cm s$^{-1}$ (Fig. D4), compared to the observed alternating jets with a meridional scale of $1.5°$ and speeds of $\sim 5$ cm s$^{-1}$ (see Figure 2 from Cravatte et al., 2012).

The performances of both Hist_Popp and Hist_Laws regarding $\delta^{13}$C$_{DIC}$ are comparable with the Norwegian Earth System Model (Tjiputra et al., 2020; comparing their Fig. 21), the UVic Earth System Model (Schmittner et al., 2013) and the Community Earth System Model (Jahn et al., 2015; comparing their Figs. 5 and 6 to our Figs. 7 and 6, respectively). The latter two

355  studies used the same $\delta^{13}$C$_{DIC}$ dataset for model evaluation. Schmittner et al. (2013) reported a better performance ($r = 0.88$ and NRMSE $= 0.5$) than ours ($r = 0.81$ and NRMSE $= 0.7$ in Hist_Popp). One main reason is that the 'nutrient trapping' problem in HAMOCC does not occur in the simulations of Schmittner et al. (2013). Our model shows noticeable better performance than that of Dentith et al. (2020). The latter study simulates too high $\delta^{13}$C$_{DIC}$ over all depth levels, which the authors ascribe to underlying biases in the biological carbon cycle.

360  # 4  Oceanic $^{13}$C Suess effect

## 4.1  Evaluation of the simulated oceanic $^{13}$C Suess effect

The oceanic $\delta^{13}$C measurements taken during the late 20th century already include a signal that originates from burning of isotopically light fossil fuel over the industrial period. The associated decrease in atmospheric $\delta^{13}$C (Fig. 2) affects oceanic $\delta^{13}$C via air-sea gas exchange, leading to a generally decrease of $\delta^{13}$C$_{DIC}$. The distribution of this $\delta^{13}$C$_{DIC}$ change, i.e. the oceanic

365  $^{13}$C Suess effect, could serve as benchmark for ocean models to evaluate the uptake and re-distribution of the anthropogenic CO$_2$ emissions in the ocean.

The model is able to reproduce the size of the global oceanic anthropogenic CO$_2$ sink. The simulated sink by year 1994 is 99 Pg C, which compares well to the observation-based estimate of $118 \pm 19$ Pg C from Sabine et al. (2004) and to other model estimates (e.g. 94 Pg C in Tagliabue and Bopp, 2008). For a direct comparison to published studies, we calculate the oceanic

370  $\delta^{13}$C Suess effect, $\delta^{13}$C$_{SE}$, as the difference between the 1990s-averaged $\delta^{13}$C$_{DIC}$ from Hist_Popp and the pre-industrial climatological (50-year mean) $\delta^{13}$C$_{DIC}$ from PI_Popp. $\delta^{13}$C$_{SE}$ calculated using the results of Hist_Laws and PI_Laws only shows marginal difference (global-mean $< 0.04$‰), and is therefore not presented. The surface mean $\delta^{13}$C$_{SE}$ in this study is $-0.66$‰, similar to the model study of Schmittner et al. (2013) ($-0.67$‰) and to the estimate by Sonnerup et al. (2007) ($-0.76 \pm 0.12$‰) who used an observation-based approach. The spatial distributions of $\delta^{13}$C$_{SE}$ show expected patterns along the vertical sec-

375  tions A16, P19 and I8S9N (Figs. 10a - 10c) and are similar to those in Eide et al. (2017a)'s estimate (Figs. 10d - 10f). The strongest oceanic $^{13}$C Suess effect is found in the subtropical gyres, where water masses have long residence times at the ocean surface and therefore receive a strong anthropogenic imprint (Quay et al., 2003). At the surface of the subtropical gyres, our simulated $\delta^{13}$C$_{SE}$ generally varies between $-0.8$ and $-1.1$‰, which compares well to the the surface ocean $\delta^{13}$C decrease of

$-0.9 \pm 0.1$‰ recorded by coral and sclerosponges (Wörheide, 1998; Böhm et al., 1996, 2000; Swart et al., 2002, 2010) and to

380 the estimates of $-1.0 \pm 0.09$‰ extracted from GLODAPv2 (Olsen et al., 2016; Eide et al., 2017a). In the subtropical gyres of the South Atlantic, the Pacific and the Indian Ocean, $\delta^{13}C_{SE}$ is mainly confined to upper 1000 m depth. In the North Atlantic, $\delta^{13}C_{SE}$ penetrates deeper than the other ocean regions, due to the intensive ventilation related to the formation of NADW. One noticeable discrepancy between the simulated $\delta^{13}C_{SE}$ and the estimates of Eide et al. (2017a) is some local positive $\delta^{13}C_{SE}$ values occur in our model. This difference will be discussed in Section 4.2.
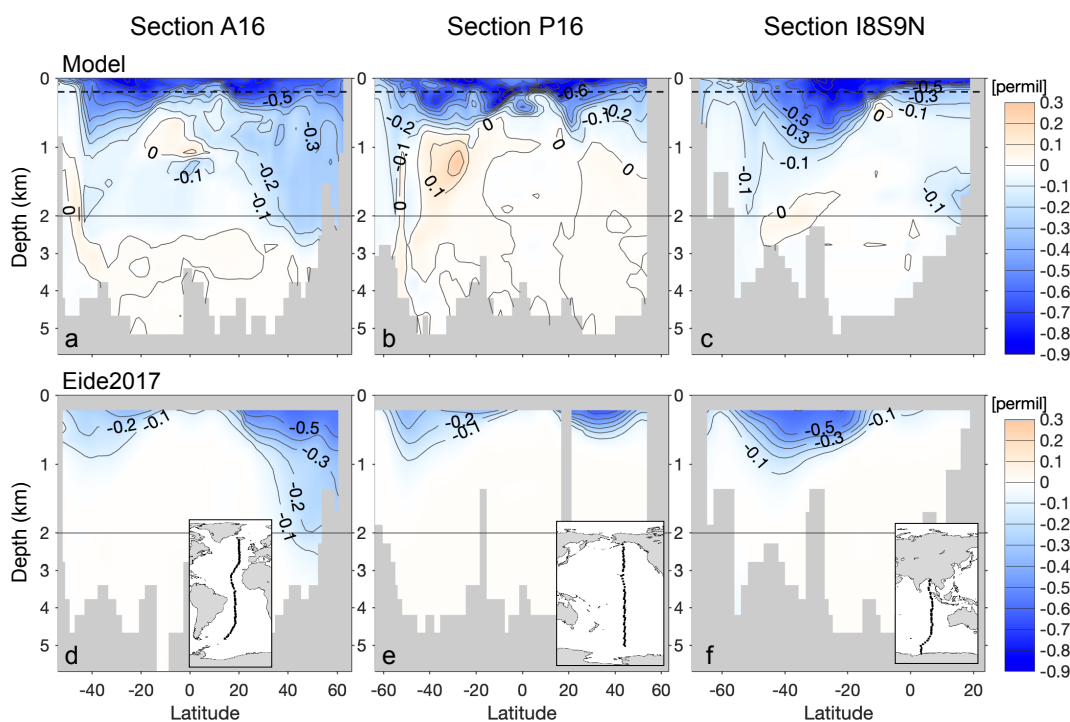
**Figure 10.** The simulated oceanic Suess effect $\delta^{13}C_{SE}$ since pre-industrial times for vertical sections A16 in the Atlantic Ocean (a), P16 in the Pacific Ocean (b) and I8S9N in the Indian Ocean (c). (d-f): as (a-c), but for the observation-based estimate of oceanic Suess effect from Eide et al. (2017a). Inserted maps show the location of the vertical sections. The horizontal dashed black lines in panels a-c indicate 200 m depth, below which Eide et al. (2017a)'s estimate is available. Note the bathymetry is different between the model and Eide et al. (2017a).

385 **4.2 Investigation of potential uncertainties in the observation-based global oceanic $^{13}$C Suess effect estimate**

To derive the global oceanic $^{13}$C Suess effect, Eide et al. (2017a) (hereafter E17) first applied the two-stage back-calculation method developed by Olsen and Ninnemann (2010) to calculate $^{13}$C Suess effect using data from the World Ocean Circulation Experiment sections. Next they mapped these $^{13}$C Suess effect estimates over a 1x1 degree grid with 24 vertical layers and obtained the three-dimension distribution of $^{13}$C Suess effect in the global ocean. For simplicity, hereafter the above procedure

390 is collectively referred to as E17's approach. E17 have noted their outcome is likely to underestimate the oceanic $^{13}$C Suess

effect by 0.15 to $0.24‰$ 200 m, globally. However, they can not provide a quantitative explanation for the sources of the underestimation.

As our model reasonably reproduces the anthropogenic $CO_2$ uptake and $\delta^{13}C_{SE}$ distribution in the ocean and it includes all necessary variables (such as $DI^{13}C$, CFC-12) required in E17's approach, we are able to investigate such potential underesti-

395 mation by applying E17's approach to our model data. Specifically, we aim to extract information on the spatial distribution of the potential underestimation and to quantitatively explain the causes for the underestimation. Below we briefly present the key assumptions and equations of E17's approach. A detailed description for E17's approach is given in Appendix C.

E17 assumed the oceanic $^{13}C$ Suess effect at any time $t$ after 1940 is proportional to CFC-12 partial pressure (pCFC-12):

$$\delta^{13}C_{SE(t-1940)} \sim a \cdot \text{pCFC-12}_t. \tag{15}$$

400 Here the proportionality factor $a$ is time-invariant. By decomposing $\delta^{13}C_{DIC}$ into a preformed component $\delta^{13}C^{pref}$ arising from the transport of the surface water with specific DIC and $DI^{13}C$ and a regenerated component $\delta^{13}C^{reg}$ due to organic matter remineralization and calcium carbonate dissolution, the following equation is derived:

$$\delta^{13}C_t^{pref} = \delta^{13}C_{SE(t-1940)} - (\delta^{13}C_t^{reg} - \delta^{13}C_{1940}^{reg}) + \delta^{13}C_{1940}^{pref}. \tag{16}$$

The calculation of $\delta^{13}C_t^{pref}$ and $\delta^{13}C_t^{reg}$ are detailed in Appendix C. Then E17 assumed the regenerated component is constant

405 in time, i.e. $\delta^{13}C_t^{reg} = \delta^{13}C_{1940}^{reg}$, which gives:

$$\delta^{13}C_t^{pref} = \delta^{13}C_{SE(t-1940)} + \delta^{13}C_{1940}^{pref}. \tag{17}$$

Combining Eq. (15) and Eq. (17), together with regarding the preformed component for year 1940, $\delta^{13}C_{1940}^{pref}$, as a term independent of pCFC-12, yields a linear relationship between the preformed component $\delta^{13}C_t^{pref}$ and pCFC-12$_t$:

$$\delta^{13}C_t^{pref} \sim a \cdot \text{pCFC-12}_t + b. \tag{18}$$

410 The regression coefficients $a$ and $b$ are determined with $\delta^{13}C_t^{pref}$ and pCFC-12$_t$ from measurement deeper than 200 m depth (below which the approach applies). With $a$ and observed pCFC-12$_t$, $\delta^{13}C_{SE(t-1940)}$ on the ocean observation sections is obtained using Eq. (15). To scale $\delta^{13}C_{SE(t-1940)}$ to $\delta^{13}C_{SE(t-PI)}$ for the full industrial period, the assumption is used that the oceanic $\delta^{13}C_{DIC}$ change scales with the atmospheric $\delta^{13}CO_2$ change, i.e.:

$$\delta^{13}C_{SE(t-PI)} = f_{atm} \cdot \delta^{13}C_{SE(t-1940)} = f_{atm} \cdot a \cdot \text{pCFC-12}_t, \tag{19}$$

415    with

$$f_{\text{atm}} = \frac{\delta^{13}\text{CO}_{2,t} - \delta^{13}\text{CO}_{2,\text{PI}}}{\delta^{13}\text{CO}_{2,t} - \delta^{13}\text{CO}_{2,1940}}. \tag{20}$$

To achieve a result comparable to E17, we select the model data at the locations for which both CFC-12 and $\delta^{13}\text{C}_{\text{DIC}}$ measurements are available. Here we use the observations compiled by Schmittner et al. (2013) because $\delta^{13}\text{C}_{\text{DIC}}$ in this data set has been quality controlled and is publicly available. The only difference with respect to the observational data used in E17

420    is that Schmittner et al. (2013) do not include the data at one South Atlantic section (A13.5) measured in 2010. However, this difference does not affect our analysis. Vertically, we use data at the model layers above the simulated pCFC-12 penetration depth (set at 20 patm, following E17). We take $t = 1994$ and perform the linear regression of Eq. (18) for five ventilation regions (the North Atlantic, South Atlantic, North Pacific, South Pacific and Indian Ocean), respectively.

The regressional relationships between $\delta^{13}\text{C}_{1994}^{\text{pref}}$ and pCFC-12$_{1994}$ (Eq. 18) and the regression coefficients, hereafter re-

425    ferred to as $a_{\text{pref}}$ and $b_{\text{pref}}$, are shown in Fig. D5 (the water masses in this figure are defined in Table D1). The coefficient of determination $r^2$, the percentage of the variance in the data explained by the regressional relationship, ranges between 0.33 and 0.66. The strength of these linear relationships is acceptable considering the lowest $r^2 = 0.22$ in E17. Applying Eq. (19) to the three-dimension model data of pCFC-12$_{1994}$ for $t = 1994$, $a_{\text{pref}}$ and $f_{\text{atm}} = 1.5$, we obtain the estimate of the global oceanic $^{13}$C Suess effect in year 1994, which we refer to as SE$_{\text{pref}}$.

430    To quantify if SE$_{\text{pref}}$ under- or overestimate the oceanic $^{13}$C Suess effect, we compare SE$_{\text{pref}}$ to the simulated oceanic $^{13}$C Suess effect in 1994 (SE$_{\text{Mod}}$). Figures 11a and 12a - 12c present (SE$_{\text{pref}}$ − SE$_{\text{Mod}}$) for 200 m depth and for the selected ocean vertical sections. Positive values of (SE$_{\text{pref}}$ − SE$_{\text{Mod}}$) indicate underestimation of the oceanic $^{13}$C Suess effect.

At 200 m SE$_{\text{pref}}$ mostly underestimates SE$_{\text{Mod}}$ (Fig. 11a). The ventilation region-mean underestimation is 0.24‰ for the Indian Ocean, 0.21‰ for the North Pacific, 0.26‰ for the South Pacific, 0.1‰ for the North Atlantic and 0.14‰ for the South

435    Atlantic (Table 1). These findings confirm the underestimation range discussed by E17. Note that E17 deduced the range of 0.15 to 0.24‰ by comparing their global-mean estimate ($-0.4$‰ at 200 m depth) to previous model studies. Specifically, based on Broecker and Peng (1993) and Bacastow et al. (1996) E17 assumed an ocean-to-atmosphere ratio of the $^{13}$C Suess effect of 0.65 and the 200 m-to-surface ratio of the $^{13}$C Suess effect of 0.6-0.7. Multiplying the above two ratios with the atmospheric $\delta^{13}\text{CO}_2$ decrease of $-1.4$‰ by year 1994 yields global-mean $^{13}$C Suess effect -0.55 to $-0.64$‰ at 200 m. In our model, the

440    global-mean ocean-to-atmosphere ratio of the $^{13}$C Suess effect is 0.46, significantly lower than the five-box model of Broecker and Peng (1993). On the other hand, our model shows a slightly higher 200 m-to-surface ratio of the $^{13}$C Suess effect (0.75) than Bacastow et al. (1996) who employed an ocean general circulation model with coarse vertical resolution (4 layers for the upper 200 m).

E17 have speculated that the major cause of the underestimation of oceanic $^{13}$C Suess effect is that the available observations

445    are mostly from the intermediate and deep waters. The ocean-atmosphere equilibration timescale for $\delta^{13}$C (10 years, Broecker and Peng, 1974) is significantly longer than that of pCFC-12 (1 month, Gammon et al., 1982). Thus, waters that have shorter surface residence time, such as the deep waters ventilated in the South Hemisphere, would show less negative slope $a_{\text{pref}}$
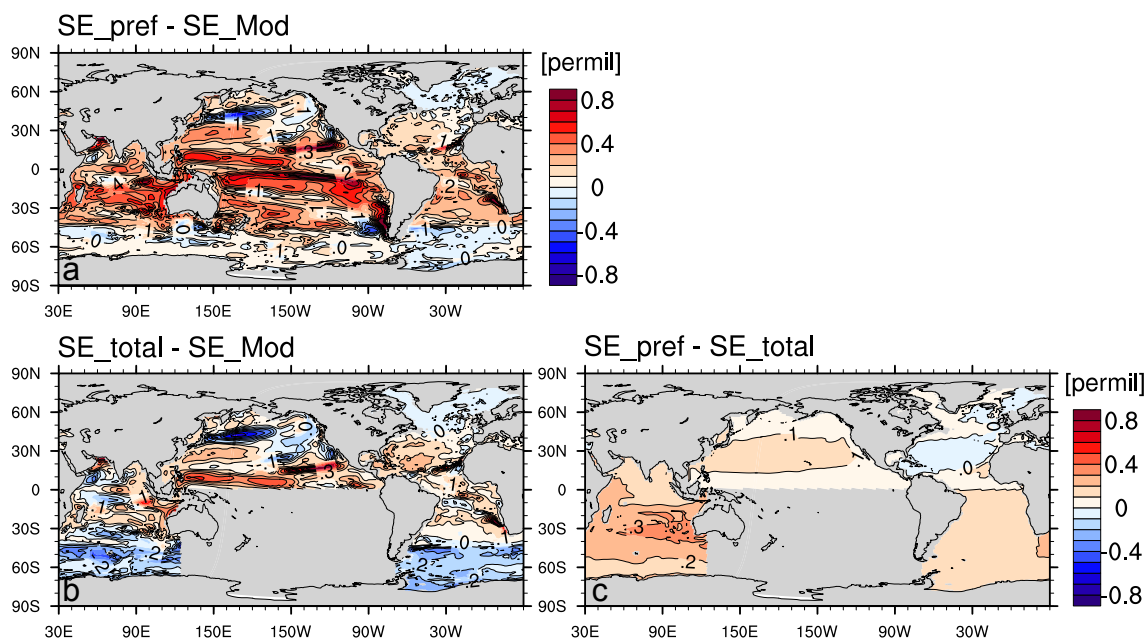
**Figure 11.** Distribution at 200 m depth for $SE_{pref} - SE_{Mod}$ (a), $SE_{total} - SE_{Mod}$ (b) and $SE_{pref} - SE_{total}$ (c). The isoline increment is $0.1‰$. In panels b and c, the South Pacific Ocean is not presented because the relationship between the total oceanic $^{13}$C Suess effect $\delta^{13}C_{SE(1994-1940)}$ and pCFC-12$_{1994}$ is too weak ($r^2 = 0.07$) and therefore $SE_{total}$ can not be estimated.

**Table 1.** Region-mean $(SE_{pref} - SE_{Mod})$, $(SE_{total} - SE_{Mod})$ and $(SE_{pref} - SE_{total})$ for the Indian, North Pacific, South Pacific, North Atlantic and South Atlantic Ocean. The unit is permil.

|  | $(SE_{pref} - SE_{Mod})$ | $(SE_{total} - SE_{Mod})$ | $(SE_{pref} - SE_{total})$ |
|---|---|---|---|
| Indian | 0.24 | 0.01 | 0.23 |
| North Pacific | 0.21 | 0.13 | 0.09 |
| South Pacific | 0.26 | \ | \ |
| North Atlantic | 0.1 | 0.09 | 0.02 |
| South Atlantic | 0.14 | -0.01 | 0.15 |

than waters that have longer surface residence time, e.g. subtropical gyres. In other words, $a_{pref}$ for water masses such as the Subtropical Gyre Water should be more negative than that for the corresponding ventilation region. Here we test this hypothesis

450     for the Indian Ocean and North Pacific Ocean. We can span regressional relationships for the subtropical gyres of these two ventilation regions because our model has higher vertical resolution in the upper ocean and therefore has more data points than field measurements. For the Indian Ocean, we combine the model data from Subtropical Gyre Water and Sub-Antarctic Mode Water as both water masses have a strong $^{13}$C Suess effect (E17). We find in the Indian Ocean $a_{pref}$ for the Subtropical Gyre Water and Sub-Antarctic Mode Water ($-0.65 \times 10^{-3}$, $r^2 = 0.49$) is more negative than that for the whole ventilation
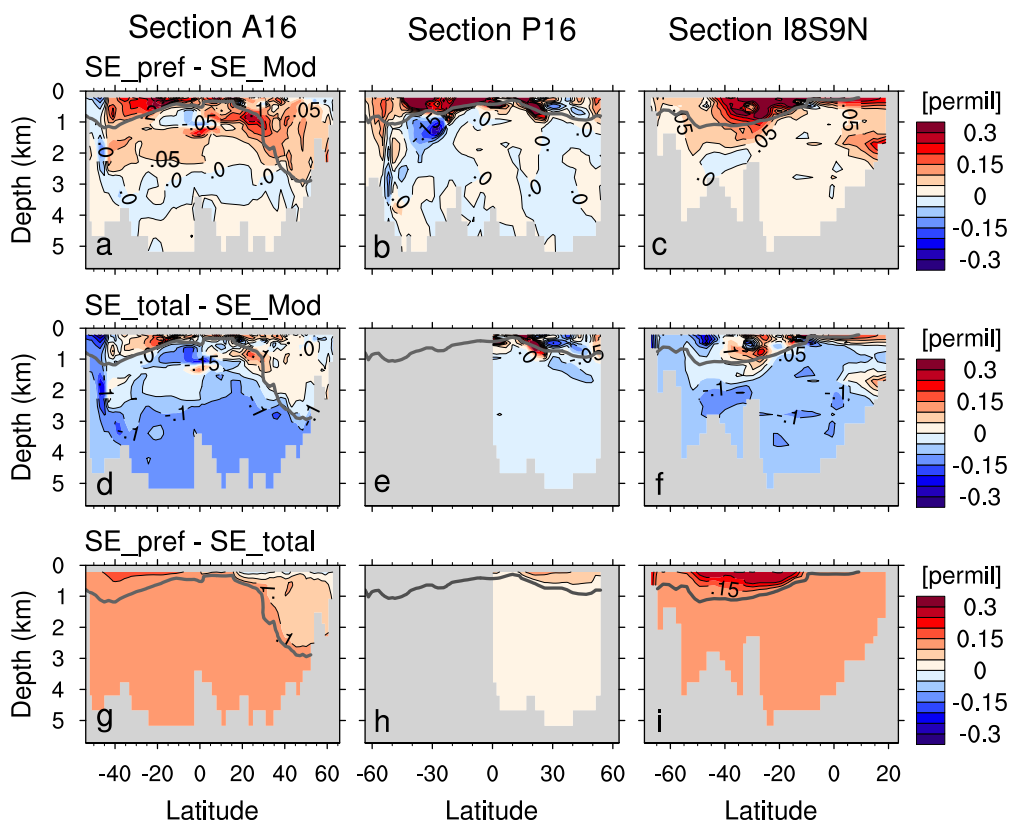
**Figure 12.** The difference $(\mathrm{SE_{pref}} - \mathrm{SE_{Mod}})$ for the vertical sections A16 in the Atlantic Ocean (a), P16 in the Pacific Ocean (b) and I8S9N in the Indian Ocean (c). (d - f) and (g - i): as (a - c), but for $(\mathrm{SE_{total}} - \mathrm{SE_{Mod}})$ and $(\mathrm{SE_{pref}} - \mathrm{SE_{total}})$, respectively. The isoline increment is $0.05‰$. The thick grey line is $\mathrm{pCFC\text{-}12_{1994}} = 20$ patm isoline, below which $\mathrm{SE_{pref}}$ is generally very small $(< 0.05‰)$.

455    region $(-0.47 \times 10^{-3})$. However, this difference in $a_{\mathrm{pref}}$ only corresponds to an underestimation of $0.12‰$ at 200 m for this subtropical region, which could not explain the total underestimation of $\Delta\delta^{13}\mathrm{C_{SE(1994-PI)}} = 0.24‰$ in the Indian Ocean. Here $0.12‰$ is calculated as $f_{\mathrm{atm}} \cdot ((-0.47 \times 10^{-3}) - (-0.65 \times 10^{-3})) \cdot \mathrm{pCFC\text{-}12_{1994}^{STGW}}$ (see Eq. 19), with $\mathrm{pCFC\text{-}12_{1994}^{STGW}} = 440$ patm being the mean pCFC-12 in the Indian subtropical region at 200 m. In the North Pacific Ocean $a_{\mathrm{pref}}$ for the Subtropical Gyre Water $(-0.44 \times 10^{-3}, r^2 = 0.26)$ is less negative than that for the whole ventilation region $(-0.71 \times 10^{-3})$ in the model, in

460    contrast to the conjecture of E17.

     To reveal the source for the underestimation, we divide $(\mathrm{SE_{pref}} - \mathrm{SE_{Mod}})$ into two components $(\mathrm{SE_{pref}} - \mathrm{SE_{total}})$ and $(\mathrm{SE_{total}} - \mathrm{SE_{Mod}})$. Here $\mathrm{SE_{total}}$ is derived similarly to $\mathrm{SE_{pref}}$ and it is based on linear regression relationships between $\delta^{13}\mathrm{C_{SE(1994-1940)}}$ and $\mathrm{pCFC\text{-}12_{1994}}$. Positive values of $(\mathrm{SE_{pref}} - \mathrm{SE_{total}})$ show the underestimation of oceanic $^{13}\mathrm{C}$ Suess effect induced by using $a_{\mathrm{pref}} \cdot \mathrm{pCFC\text{-}12_{1994}}$ to approximate the relationship between the $\delta^{13}\mathrm{C_{SE(1994-1940)}}$ and pCFC-12. The difference $(\mathrm{SE_{total}} -$

465    $\mathrm{SE_{Mod}})$ shows how well a method based on linear relationships between the $\delta^{13}\mathrm{C_{SE(1994-1940)}}$ and $\mathrm{pCFC\text{-}12_{1994}}$ can estimate the global ocean $^{13}\mathrm{C}$ Suess effect.

To calculate $SE_{total}$ we perform a linear regression for the total oceanic $^{13}C$ Suess effect $\delta^{13}C_{SE(1994-1940)}$ and pCFC-12$_{1994}$ with the subsampled model data:

$$\delta^{13}C_{SE(1994-1940)} \sim a_{total} \cdot \text{pCFC-12}_{1994} + b_{total}. \tag{21}$$

470   This is followed by scaling from the period 1940 - 1994 to the full industrial period in analogy to Eq. (19):

$$SE_{total} = f_{atm} \cdot (a_{total} \cdot \text{pCFC-12}_{1994} + b_{total}). \tag{22}$$

The regression relationships in Eq. (21) and regression coefficients are given in Fig. D6. For the Indian, North Pacific, North Atlantic and South Atlantic Ocean, $r^2$ lies between 0.34 and 0.67, which suggests acceptable strength of the relationships. In the South Pacific Ocean we find low $r^2 = 0.07$, and therefore we don't compute $SE_{total}$ for the South Pacific Ocean. The causes

475   for this low $r^2$ will be discussed later in this section.

With Eqs. (19) and (22) we get

$$SE_{pref} - SE_{total} = f_{atm} \cdot (a_{pref} - a_{total}) \cdot \text{pCFC-12}_{1994} - f_{atm} \cdot b_{total}. \tag{23}$$

$(SE_{total} - SE_{Mod})$ at 200 m generally show positive values, i.e. underestimation, in low latitudes (between $40°$ S and $40°$ N) and it is rather negative poleward of $40°$ (Fig. 11b). This pattern results from lumping together data from different water masses

480   to generate one regression relationship for a large ventilation region. The waters ventilated in lower latitudes typically have stronger $^{13}C$ Suess effect than those ventilated in high latitudes. This is clearly reflected in the linear regression relationships between $\delta^{13}C_{SE(1994-1940)}$ and pCFC-12$_{1994}$ for the North Atlantic Ocean (Fig. D6d), which shows the regression slope $a_{total}$ for the Subtropical Gyre Water is noticeably steeper than that of the deep waters. Accordingly in the interior ocean, the water masses ventilated in the low latitudes generally show underestimation of $^{13}C$ Suess effect (positive values of $SE_{total} - SE_{Mod}$)

485   and the water masses ventilated in the high latitudes show overestimation (Figs. 12d - 12f). In the North Atlantic Ocean, the region-mean underestimation $SE_{pref} - SE_{Mod} = 0.1‰$ is predominantly contributed by $SE_{total} - SE_{Mod} = 0.09‰$. In the North Pacific Ocean $SE_{total} - SE_{Mod} = 0.13‰$ accounts for more than half of the total underestimation $0.21‰$. In the Indian and South Atlantic Ocean, however, $(SE_{total} - SE_{Mod})$ has hardly any influence to the region-mean underestimation.

In the South Atlantic, North Pacific and Indian Ocean, $(SE_{pref} - SE_{total})$ is always positive and it decreases with increasing

490   depth (Figs. 11c, 12g - 12i) because pCFC-12 decreases towards the interior ocean (see Eq. 23). In the South Atlantic and Indian Ocean, $(SE_{pref} - SE_{total})$ determines the region-mean underestimation (Table 1). In the North Pacific Ocean, it contributes to less than half of the underestimation (Table 1). We find two main causes of the underestimation from the component $(SE_{pref} - SE_{total})$ in the above three regions. The first arises from the assumption that $\delta^{13}C_{1940}^{pref}$ is a constant in the regression equation Eq. (18). As is shown for the zonal-averaged vertical sections, $\delta^{13}C_{1940}^{pref}$ exhibits noticeable spatial variations (Figs. 13a

495   - 13c). Over a considerable fraction of ocean regions (e.g. north of $40°$ S in the South Atlantic Ocean, south of $35°$ N in the North Pacific Ocean, north of $40°$ S in the Indian Ocean) $\delta^{13}C_{1940}^{pref}$ generally decreases with increasing depth. This vertical

distribution is similar to that of pCFC-12$_{1994}$ (Figs. 13d - 13f). Such a seemingly positive correlation between $\delta^{13}C^{\text{pref}}_{1940}$ and pCFC-12$_{1994}$ exists because during the pre-industrial times, in our model the preformed component $\delta^{13}C^{\text{pref}}$ generally decreases with increasing water depth, which has also been reported by Schmittner et al. (2013) (see their Figs. 5 and 6). In the

500 industrial period prior to 1940, the decrease of the atmospheric $^{13}C/^{12}C$ ratio is relatively slow (Fig. 2). Thus, by the year 1940 the oceanic uptake of isopotically light $CO_2$ only partly offsets vertical gradient of the pre-industrial $\delta^{13}C^{\text{pref}}$. Consequently, the seemingly positive correlation between $\delta^{13}C^{\text{pref}}_{1940}$ and pCFC-12$_{1994}$ results in less negative $a_{\text{pref}}$ than $a_{\text{total}}$. This therefore generates the underestimation of $^{13}C$ Suess effect in the South Atlantic, North Pacific and Indian Ocean in the model.
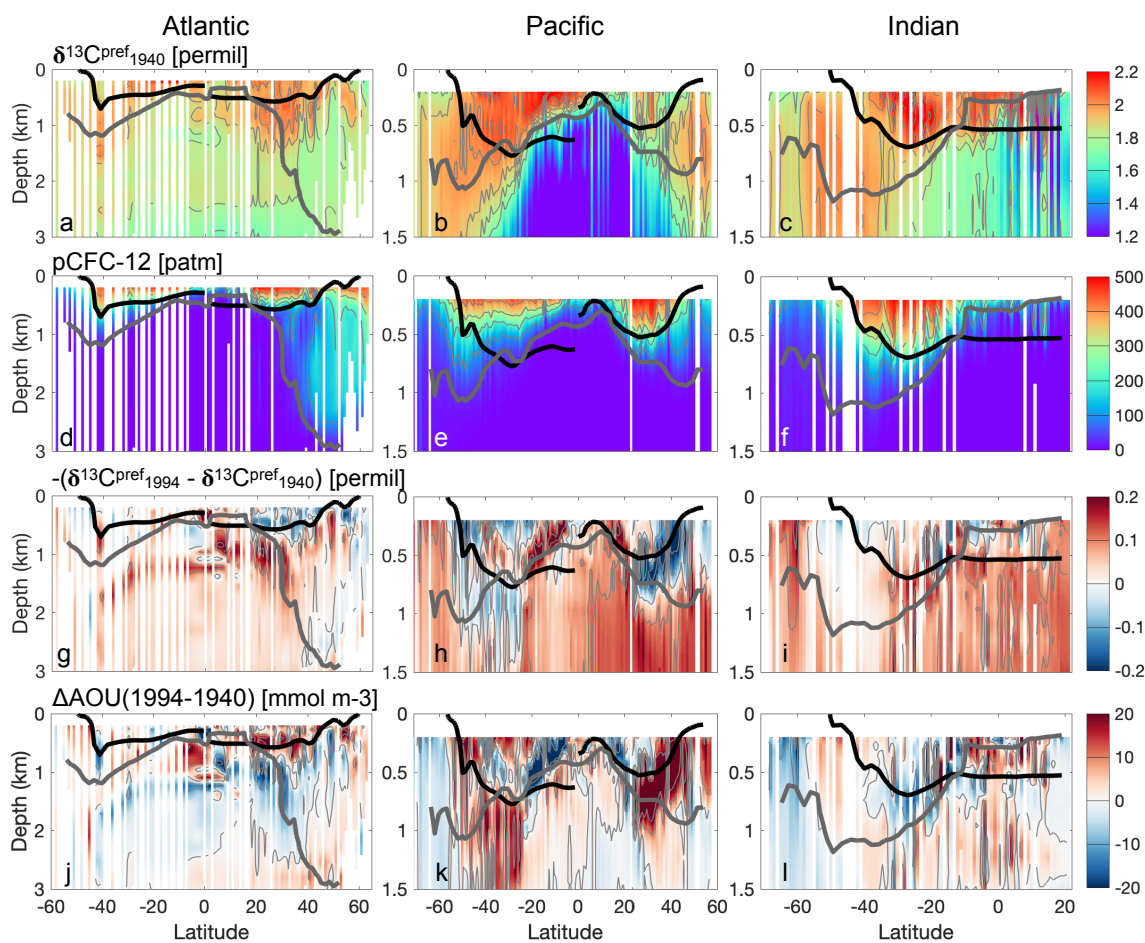
**Figure 13.** (a - c): The zonal mean of the simulated $\delta^{13}C^{\text{pref}}_{1940}$ for the locations where both observed CFC-12 and $\delta^{13}C_{\text{DIC}}$ are available. The thick grey line is pCFC-12$_{1994}$ = 20 patm isoline, above which model data is used to perform linear regression. The thick black lines outline the Subtropical Gyre Water in the Atlantic and North Pacific Ocean, the Subtropical Gyre Water and Sub-Antarctic Mode Water in the Indian Ocean and South Pacific ocean (definition of water masses in Table D1). (d - f), (g - i) and (j - l): as (a - c), but for pCFC-12$_{1994}$, for $-(\delta^{13}C^{\text{reg}}_{1994} - \delta^{13}C^{\text{reg}}_{1940})$ and for AOU changes between year 1940 and 1994, respectively. Note that for the Atlantic Ocean the upper 3 km is shown, whereas for the Pacific and Indian Ocean the upper 1.5 km is presented.

The second cause for the underestimation in the component $(\text{SE}_{\text{pref}} - \text{SE}_{\text{total}})$ is that $\delta^{13}\text{C}_{\text{SE}(1994-1940)}$ is set to zero in the
505   waters pCFC-12$_{1994}$ = 0 (Eq. 15). However, this assumption does not always hold because of the longer atmospheric time
history of $^{13}$C Suess effect than CFC-12, as is already discussed by E17. This point is supported by non-negligible values
of the regression intercept $b_{\text{total}}$ in our study. In the South Atlantic and Indian Ocean, $b_{\text{total}} = -0.07\%o$ corresponds to an
underestimation of $0.11\%o$ ($= -f_{\text{atm}} \cdot b_{\text{total}}$, see Eq. 23). Thus, neglecting $^{13}$C Suess effect in CFC-12 water contributes to
almost half of the total underestimation at 200 m for the Indian Ocean and it contributes to about 80% for the South Atlantic
510   Ocean (Table 1).

Different from the previously discussed three ventilation regions, in the North Atlantic Ocean negative $(\text{SE}_{\text{pref}} - \text{SE}_{\text{total}})$ is
found at 200 m (Fig. 11c), which becomes positive below about 250 m (Fig. 12g). The reason is $a_{\text{pref}} = -0.81 \times 10^{-3}$ is more
negative than $a_{\text{total}} = -0.62 \times 10^{-3}$ (Figs. D5d and D6d). This is related to the assumption that the regenerated component
of $\delta^{13}\text{C}_{\text{DIC}}$ is constant in time, i.e. $-(\delta^{13}\text{C}^{\text{reg}}_{1994} - \delta^{13}\text{C}^{\text{reg}}_{1940}) = 0$ in Eq. (16). As is shown by Figs. 13g - 13i, $-(\delta^{13}\text{C}^{\text{reg}}_{1994} -$
515   $\delta^{13}\text{C}^{\text{reg}}_{1940})$ is non-negligible, with the magnitude up to $0.3\%o$. Above 1500 m, the spatial variability of $-(\delta^{13}\text{C}^{\text{reg}}_{1994} - \delta^{13}\text{C}^{\text{reg}}_{1940})$
can be mainly attributed to the change of organic matter remineralization in the ocean interior, as is illustrated by the tem-
poral change of AOU (Figs. 13j - 13l). Below 1500 m, the $\delta^{13}\text{C}^{\text{reg}}$ changes are generally negative (Figs. D7d - D7f) be-
cause $\delta^{13}\text{C}_{\text{POC}}$ decreases globally by about $1.3\%o$ during 1940-1994 (Fig. D8), mainly due to the decline of the biological
fractionation factor $\epsilon_{\text{p}}$ under increasing surface $\text{CO}_2(\text{aq})$. In the North Atlantic Ocean, $-(\delta^{13}\text{C}^{\text{reg}}_{1994} - \delta^{13}\text{C}^{\text{reg}}_{1940})$ is mostly
520   negative above 500 m, where pCFC-12$_{1994}$ is relatively high (Fig. 13g). Below 500 m, where pCFC-12$_{1994}$ is relatively
low, $-(\delta^{13}\text{C}^{\text{reg}}_{1994} - \delta^{13}\text{C}^{\text{reg}}_{1940})$ is mostly positive. Thus, an apparent negative correlation between the spatial distributions of
$-(\delta^{13}\text{C}^{\text{reg}}_{1994} - \delta^{13}\text{C}^{\text{reg}}_{1940})$ and pCFC-12$_{1994}$ leads to a more negative $a_{\text{pref}}$ than $a_{\text{total}}$, according to Eq. (16). The consequential
overestimation of $\delta^{13}\text{C}_{\text{SE}(1994-\text{PI})}$ by $0.09\%o$ ($= f_{\text{atm}} \cdot (a_{\text{pref}} - a_{\text{total}}) \cdot$ pCFC-12$_{1994}$) is compensated by a underestimation of
$0.12\%o$ ($= -f_{\text{atm}} \cdot b_{\text{total}}$) due to the negative linear regression intercept $b_{\text{total}} = -0.08\%o$. Overall we find a negligible underesti-
525   mation of mean $(\text{SE}_{\text{pref}} - \text{SE}_{\text{total}}) = 0.02\%o$ at 200 m depth in the North Atlantic Ocean.

The temporal change of $\delta^{13}\text{C}^{\text{reg}}$ also causes the positive values of $\delta^{13}\text{C}_{\text{SE}}$ at depth, for instance, below 1000 m on the vertical
section P16 in the South Pacific Ocean (Fig. 10b). Here the positive change of $\delta^{13}\text{C}^{\text{reg}}$ is due to a decrease of remineralisation,
as is shown by the change of AOU in this region (Fig. D8h). Hence, less negative $\delta^{13}\text{C}_{\text{POC}}$ signal is released in this region and
$\delta^{13}\text{C}_{\text{DIC}}$ slightly increases.

530   We don't compute $\text{SE}_{\text{total}}$ for the South Pacific Ocean because of a low $r^2 = 0.07$ obtained for the linear regression between
$\delta^{13}\text{C}_{\text{SE}(1994-1940)}$ and pCFC-12$_{1994}$, suggesting no linear relation between the two variables (Fig. D6c). The model data for the
Subtropical Gyre Water and the Antarctic Intermediate Water in the South Pacific Ocean are particularly scattered (Fig. D5f)
because $-(\delta^{13}\text{C}^{\text{reg}}_{1994} - \delta^{13}\text{C}^{\text{reg}}_{1940})$ shows significant spatial variability within each of these two water masses (Fig. D7e). These
changes of $\delta^{13}\text{C}^{\text{reg}}$ are mainly caused by the changes of ocean carbon cycle in our model, as is illustrated by the AOU
535   changes (Fig. D7h).

Although we can not directly evaluate $(\text{SE}_{\text{pref}} - \text{SE}_{\text{total}})$ for the South Pacific Ocean, we can try to understand the total
underestimation ($0.26\%o$ at 200 m, being the largest among the five ventilation regions, see Table 1) by analysing the spatial
distribution of the terms in Eq. (16). A seemingly positive correlation clearly exists between $\delta^{13}\text{C}^{\text{pref}}_{1940}$ and pCFC-12$_{1994}$, which

both decreases with increasing depth (Fig. 13b). This contributes to the underestimation of $^{13}$C Suess effect (according to
540  Eq. 23), similar to the case for the Indian, South Atlantic and North Pacific Ocean. Above the pCFC-12=20 patm isoline,
$-(\delta^{13}C^{reg}_{1994} - \delta^{13}C^{reg}_{1940})$ mostly decrease with increasing depth (Fig. 13h), similar to the Atlantic Ocean, which contributes to
an overestimation.

Note that due to inevitable model biases, our model does not perfectly reproduce the distribution and properties of the ob-
served water masses (see more discussion in Appendix C). Thus our regression relationships between $\delta^{13}C^{pref}$ and pCFC-12 (Fig. D5)
545  show some quantitative differences to those of E17 (see their Fig. 3). Nevertheless, our analysis provides a possible spatial
distribution of the underestimation of $^{13}$C in E17's product. More importantly, we uncover two major causes for the underesti-
mation: the assumption of a spatially constant $\delta^{13}C^{pref}_{1940}$ and the neglect of $^{13}$C Suess effect in CFC-12 free water.

## 5  Summary and conclusions

We present results of the new $^{13}$C module in the ocean biogeochemical model HAMOCC6 for the historical period forced
550  by reanalyses data (ERA20C). We test two parameterisations of different complexity for the biological fractionation factor:
$\epsilon^{Popp}_p$ depends on dissolved $CO_2$ (Popp et al., 1989); $\epsilon^{Laws}_p$ is a function of dissolved $CO_2$ and phytoplankton growth rate (Laws
et al., 1995). Futhermore, we used our consistent model framework to assess the approach by Eide et al. (2017a), who used
a correlation between preformed $\delta^{13}C_{DIC}$ and CFC-12 partial pressure to obtain an estimate of the global oceanic $^{13}$C Suess
effect.

555  The comparison between simulated and observed isotopic ratio of organic matter $\delta^{13}C_{POC}$ reveals that $\epsilon^{Popp}_p$ ($r = 0.84$ and
NRMSE $= 0.57$) has a better performance than $\epsilon^{Laws}_p$ ($r = 0.71$ and NRMSE $= 2.5$). Using $\epsilon^{Laws}_p$ results in noticeably lower
$\delta^{13}C_{POC}$ values and smaller $\delta^{13}C_{POC}$ gradients between low and high latitudes compared to observations. The parameterisation
of Laws et al. (1995), obtained based on cultures of marine diatom *Phaeodactylum tricornutum*, results in a too strong pref-
erence of the isotopically light carbon. Therefore it is not a good representative for $^{13}$C biological fractionation in our global
560  ocean biogeochemical model.

Regarding $\delta^{13}C_{DIC}$, $\epsilon^{Popp}_p$ yields slightly better agreement with observations than $\epsilon^{laws}_p$ ($r = 0.81$ and NRMSE $= 0.7$ ver-
sus $r = 0.80$ and NRMSE $= 1.1$), because $\epsilon^{Laws}_p$ produces larger vertical gradients of $\delta^{13}C_{DIC}$ and a lower $DI^{13}C$ inventory
than those found in observations. Nevertheless, both $\epsilon^{Popp}_p$ and $\epsilon^{laws}_p$ perform well considering the uncertainties in observed
$\delta^{13}C_{DIC}$ ($0.1 - 0.2‰$; Schmittner et al., 2013) and the model biases in the physical state (e.g. a too shallow boundary between
565  NADW cell and the Antarctic Bottom Water cell in MPIOM).

Our model well represents the temporal evolution of the oceanic $\delta^{13}C_{DIC}$ since pre-industrial times, i.e. the oceanic $^{13}$C
Suess effect due to the intrusion of isotopically light carbon into the ocean. With the complete information on the spatial and
temporal $^{13}$C evolution in the ocean, together with the simulated evolution of CFC-12, we constrain the potential uncertainties
in the framework of Eide et al. (2017a) for deriving an observation-based oceanic $^{13}$C Suess effect. Based on our model, we
570  find underestimations of $^{13}$C Suess effect at 200 m by $0.24‰$ in the Indian Ocean, $0.21‰$ in the North Pacific Ocean, $0.26‰$
in the South Pacific Ocean, $0.1‰$ in the North Atlantic Ocean and $0.14‰$ in the South Atlantic Ocean. These numbers confirm

the underestimation range 0.15 to 0.24‰ conjectured by Eide et al. (2017a). They speculated this underestimation is due to the under-representation of the water masses with stronger $^{13}$C Suess effect, such as the Subtropical Gyre Water and Sub-Antarctic Model Water, in the observational data. Our analysis shows that their hypothesis only explain half of the underestimation in

575   the Indian Ocean. For the North Atlantic Ocean this hypothesis is not supported by the model data . We identify two major causes for the underestimation of $^{13}$C Suess effect by the applied method. The first relates to the assumption that the preformed component of $\delta^{13}C_{DIC}$ in year 1940 is spatially constant, whereas it shows considerable spatial variability in our model. This preformed component also shows a seemingly positive correlation with pCFC-12, which contribute to the underestimation of $\delta^{13}$C Suess effect. The second cause relates to the neglect of the $^{13}$C Suess effect in the CFC-12 free water. This assumption

580   corresponds to an underestimation of 0.11‰ at 200 m depth in the Indian Ocean and the South Atlantic Ocean.

We conclude that the new $^{13}$C module with biological fractionation factor $\epsilon_p^{Popp}$ from Popp et al. (1989) has a satisfactory performance. Thus, our new $^{13}$C module will serve as a useful tool to evaluate the performance of MPI-ESM in paleo-climate and to investigate the past changes in the ocean, for instance within the ongoing research project PalMod (Latif et al., 2016).

## Appendix A:  Governing factors for the water-column DI$^{13}$C inventory changes

585   The water-column DI$^{13}$C inventory difference is primarily a result of the difference of the net air-sea $^{13}CO_2$ flux between PI_Popp and PI_Laws. This is demonstrated by the comparison of the contributions of the governing factors for the water-column DI$^{13}$C inventory changes (Table A1), including air-sea gas exchange, loss of POC and $CaCO_3$ to marine sediment, diffusion of the remineralised DIC from sediment into the water column, input of DOC and $CO_3^{2-}$, and the exchange with other marine carbon pools (phytoplankton, $CaCO_3$, etc.). Table A1 also reveals that the current method to determine the $^{13}$C

590   input (see Section 2.3.2) only has a small contribution to the change of the water-column DI$^{13}$C inventory.

**Table A1.** Contributions to the rate of the water-column DI$^{13}$C inventory change (in Gmol yr$^{-1}$), averaged in the last 50 years in the corresponding pre-industrial spin-up simulations. Positive values denote contributions to the increase of the water-column DI$^{13}$C inventory. Last column gives relative contribution to the total rate difference with relative contribution = (PI_Laws-PI_Popp) / total rate difference.

| 13C fluxes into the water column (Gmol yr $^{-1}$) | PI_Popp | | PI_Laws | | PI_Laws - PI_Popp | | relative contribution |
|---|---|---|---|---|---|---|---|
| air-sea gas exchange | 1824.4 | | 1552.3 | | -272.1 | | 1.1 |
| POC loss to sediment | -34902.9 | | -34626.4 | | 276.5 | | |
| CaCO$_3$ loss to sediment | -16672.1 | | -16674.3 | | -2.2 | | |
| DOC input | 13612.7 | sum: 626.6 | 13506.8 | sum: 596.1 | -105.9 | sum: 30.5 | -0.1 |
| CO$_3^{2-}$ input | 16505.2 | | 16506.9 | | 1.7 | | |
| sediment DIC reflux | 22053.2 | | 21913.6 | | -139.6 | | |
| from other water-column carbon pools | 63.8 | | 64.2 | | -0.4 | | 0.001 |
| total rate | 2484.7 | | 2242.7 | | -242.0 | | 1 |

## Appendix B: Model-observation comparison of net primary production, phytoplankton growth rate and biomass

The simulated net primary production, 48.7 Gt yr$^{-1}$ for bulk phytoplankton and 3 Gt yr$^{-1}$ for cyanobacteria, compares well with the satellite-based estimate of $\sim$ 52 Gt yr$^{-1}$ (Westberry et al., 2008; Silsbe et al., 2016). The simulated growth rate $\mu$ (Figs. B1a and B1b, only shown for bulk phytoplankton because cyanobacteria has a much lower primary production) is

595    broadly consistent with the large-scale patterns of the satellite-based $\mu$ estimates from Westberry et al. (2008) (Figs. B1c and B1d) and with field observations. In the central equatorial Pacific the simulated $\mu$ well reproduces the observed range (0.55-0.7 day$^{-1}$, Chavez et al., 1996; note the satellite-based estimates overestimate $\mu$ due to excluding iron limitation). In the subtropical gyres, the simulated $\mu$ (annual-mean 0.1-0.25 day$^{-1}$) is at the lower side of both the observations (annual mean 0.3-0.53 day$^{-1}$ in the North Pacific subtropical gyre, Letelier et al., 1996; annual mean 0.13-0.62 day$^{-1}$ in the North Atlantic

600    subtropical gyre, Marañón, 2005) and the satellite-based $\mu$ estimates. In the Pacific sector of the Southern Ocean, the simulated $\mu$ (0.3-0.4 day$^{-1}$) in the austral summer is higher than the observations (about 0.1-0.2 day$^{-1}$; Boyd et al., 2000) and the satellite-based estimates. The simulated phytoplankton biomass is too high in the equatorial Pacific ($>$ 100 mg C m$^{-3}$) and the Southern Ocean ($>$ 50 mg C m$^{-3}$; Fig. B2) compared to the satellite-based estimates ($<$ 30 mg C m$^{-3}$ for both regions; Westberry et al., 2008).
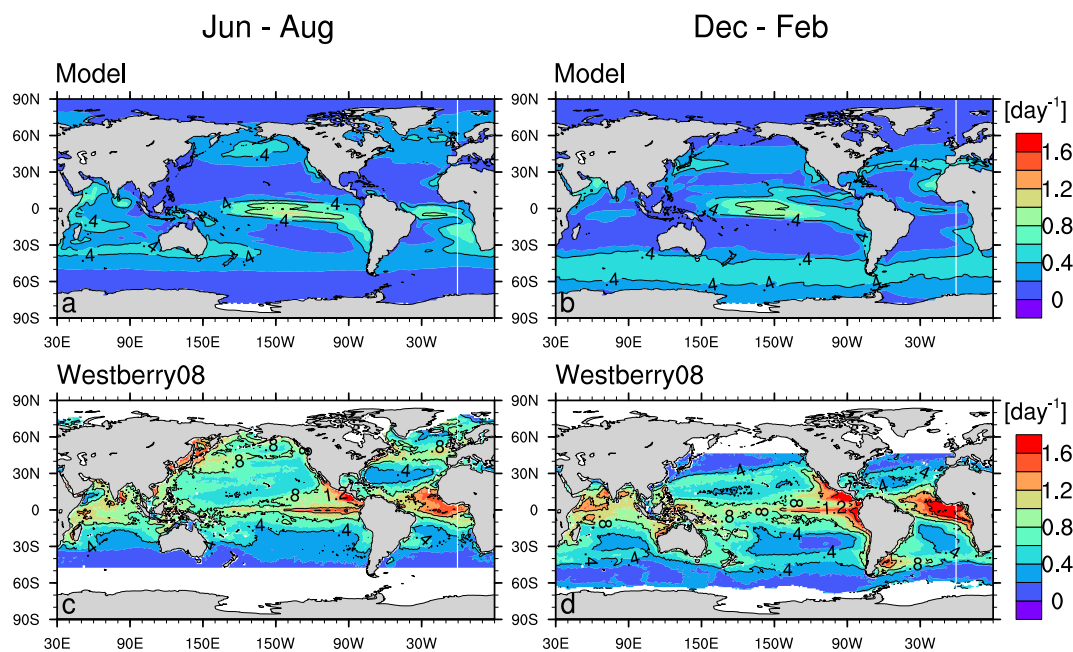
**Figure B1.** The 1999-2004 climatological-mean surface phytoplankton growth rates (day$^{-1}$) of the model (a, b, for bulk phytoplankton) and of the satellite-based estimates from Westberry et al. (2008) (c, d) for the boreal summer (left column) and winter (right column).
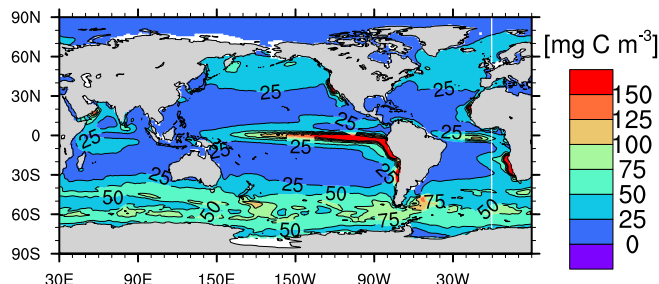
**Figure B2.** The 1999-2004 averaged annual-mean surface phytoplankton biomass (mg C m$^{-3}$) of the model.

**Appendix C: Applying Eide et al. (2017a)'s approach to the model data**

E17's procedure first assumes that any oceanic CFC-12 signal before 1940 is negligible and the oceanic $^{13}$C Suess effect at any time t after 1940 is proportional to CFC-12 partial pressure at time t:

$$\delta^{13}C_{SE(t-1940)} \sim a \cdot pCFC\text{-}12_t. \tag{C1}$$

Here the proportionality factor $a$ is time-invariant. $\delta^{13}C_{DIC}$ at any time t after year 1940 is decomposed as:

$$\delta^{13}C_t = \delta^{13}C^{pref}_{1940} + \delta^{13}C^{reg}_{1940} + \delta^{13}C_{SE(t-1940)} + \Delta\delta^{13}C^{reg} + \Delta\delta^{13}C^{pref}. \tag{C2}$$

The superscript "pref" represents the preformed component, which arises from the transport of the surface water with specific DIC and DI$^{13}$C. Superscript "reg" denotes the regenerated component $\delta^{13}C^{reg}_{SE}$ due to organic matter remineralisation and calcium carbonate dissolution. The two last terms contain any changes not related to the $^{13}$C Suess effect, e.g. changes in ocean carbon cycle. Decomposing the left-hand side of Eq. (C2) gives

$$\delta^{13}C^{pref}_t = \delta^{13}C_{SE(t-1940)} + \delta^{13}C^{pref}_{1940} - (\delta^{13}C^{reg}_t - \delta^{13}C^{reg}_{1940}) + \Delta\delta^{13}C^{reg} + \Delta\delta^{13}C^{pref}. \tag{C3}$$

Note here $-(\delta^{13}C^{reg}_t - \delta^{13}C^{reg}_{1940}) + \Delta\delta^{13}C^{reg}$ represents any change of the regenerated component and is equivalent to $-(\delta^{13}C^{reg}_t - \delta^{13}C^{reg}_{1940})$ in Eq. (16) in Section 4.2. In E17, the terms $(\delta^{13}C^{reg}_t - \delta^{13}C^{reg}_{1940})$, $\Delta\delta^{13}C^{reg}$ and $\Delta\delta^{13}C^{pref}$ are assumed zero. Combining Eq. (C1) and Eq. (C3) yields

$$\delta^{13}C^{pref}_t \sim a \cdot pCFC\text{-}12_t + b, \tag{C4}$$

where $b$ contains terms $\delta^{13}C^{pref}_{1940}$. Thus, the proportionality factor $a$ can be determined with $\delta^{13}C^{pref}_t$ and $\cdot pCFC\text{-}12_t$ at time t, and $\delta^{13}C_{SE(t-1940)}$ is obtained with Eq. (C1).

The preformed component is calculated following Sonnerup et al. (1999) and Eide et al. (2017a):

$$\delta^{13}C^{\text{pref}} = \frac{\delta^{13}C_{\text{DIC}} \cdot \text{DIC} - \text{AOU} \cdot \left(\frac{C}{-O_2}\right)_{\text{org}} \cdot \delta^{13}C_{\text{org}}}{\text{DIC} - \text{AOU} \cdot \left(\frac{C}{-O_2}\right)_{\text{org}}}. \tag{C5}$$

This equation is only valid below the 200 m, which is roughly the euphotic zone depth (E17). The $\left(\frac{C}{-O_2}\right)_{\text{org}}$ ratio is 122:172 in

625 HAMOCC6, and we use the simulated $\delta^{13}C_{\text{POC}}$ for $\delta^{13}C_{\text{org}}$. The dissolution of $CaCO_3$ is neglected following Sonnerup et al. (1999), who argued this simplification only results in a small offset ($< 2\%$).

To scale $\delta^{13}C_{\text{SE}(t-1940)}$ to $\delta^{13}C_{\text{SE}(t-\text{PI})}$ for the full industrial period, the assumption is used that the oceanic $\delta^{13}C_{\text{DIC}}$ change scales with the atmospheric $\delta^{13}CO_2$ change, i.e.:

$$\delta^{13}C_{\text{SE}(t-\text{PI})} = f_{\text{atm}} \cdot \delta^{13}C_{\text{SE}(t-1940)} = f_{\text{atm}} \cdot a \cdot \text{pCFC-12}_t, \tag{C6}$$

630 with

$$f_{\text{atm}} = \frac{\delta^{13}CO_{2,t} - \delta^{13}CO_{2,\text{PI}}}{\delta^{13}CO_{2,t} - \delta^{13}CO_{2,1940}}. \tag{C7}$$

For mapping E17 performed another linear regression for $\delta^{13}C_{\text{SE}(t-\text{PI})}$ and $\text{pCFC-12}_t$. This step is not need here as we take $t = 1994$ rather than various years from observations. To obtain three-dimention distribution of $^{13}C$ Suess effect for the global ocean, we apply Eq. (C6) to the simulated $\text{pCFC-12}_{1994}$.

635 The regression relationships between $\delta^{13}C^{\text{pref}}$ and pCFC-12 in our model (Fig. D5) show some quantitative differences to those of E17 (see their Fig. 3). The reason is our model does not perfectly reproduce the distribution and properties of the observed water masses and this can be seen in the following aspects. First, the definitions of several water masses in the model are slightly different from those of E17 (comparing our Table D1 with their Table 2). Second, our simulated $\delta^{13}C_t^{\text{pref}}$ in the deep and bottom waters (Antarctic Bottom Water, Circumpolar Deep Water, Pacific Deep Water and Indian Deep Water) in the

640 Southern Hemisphere (Figs. D5c, D5e and D6c) is higher than that in E17 (see their Figs. 3a. 3c and 3e). The possible causes for this difference are two fold. First, in the Southern Ocean deep convection, which primarily occurs in the open ocean rather than the along continental shelf, is too strong in the model. This can be seen by the large mixed layer depth (Fig. D2), and by the zonal-mean CFC-12 bias distribution (Fig. D9), which features persistent positive biases off the Antarctic continental shelf in the Atlantic, Pacific and Indian sectors of the Southern Ocean. The second cause is the Southern Ocean has a too high primary

645 production (about a factor of 1.5 of the satellite-based net primary production estimates from Westberry et al., 2008). The high primary production causes higher surface $\delta^{13}C_{\text{DIC}}$ than observations (see the South Pacific Ocean in Fig. 8c). Consequently, the simulated preformed component $\delta^{13}C_t^{\text{pref}}$ in the bottom and deep water masses of the Southern Ocean is higher than observed values in E17. Third, the lowest values of $\delta^{13}C_t^{\text{pref}}$ ($< 1.4\%$) are often found in the upwelling regions in the model. This is due to the upward transport of water from the ocean interior that has lower $\delta^{13}C_{\text{DIC}}$ than observations (Figs. 9e and 9f).

650 **Appendix D: Additional figures and tables**
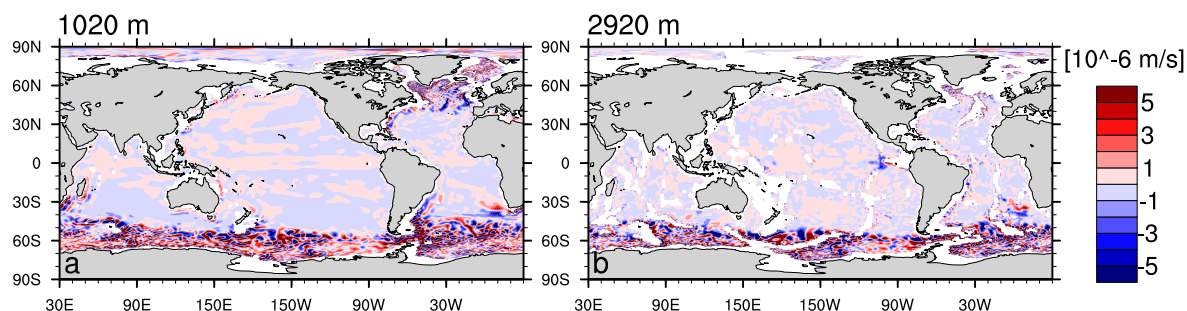
**Figure D1.** 1990-2009 mean vertical velocity (m s$^{-1}$) in the model at 1020 m (a) and 2920 m depth (b).
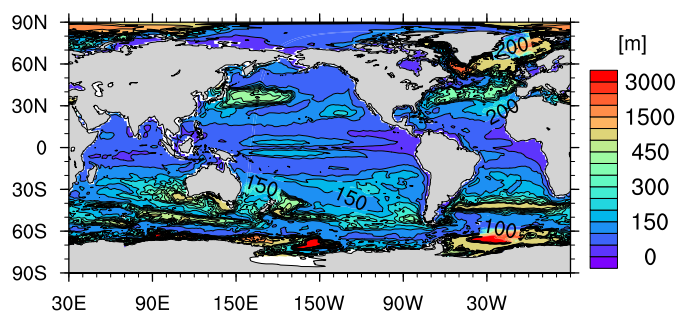
**Figure D2.** Maximum climatological (1970-1999) monthly mean mixed layer depth (m) in the model. The mixed layer depth is defined as the depth at which a 0.03 kg m$^{-3}$ change of potential density with respect to the surface has occurred. Contour intervals are 50 for 0-500, 500 for 500-3000.
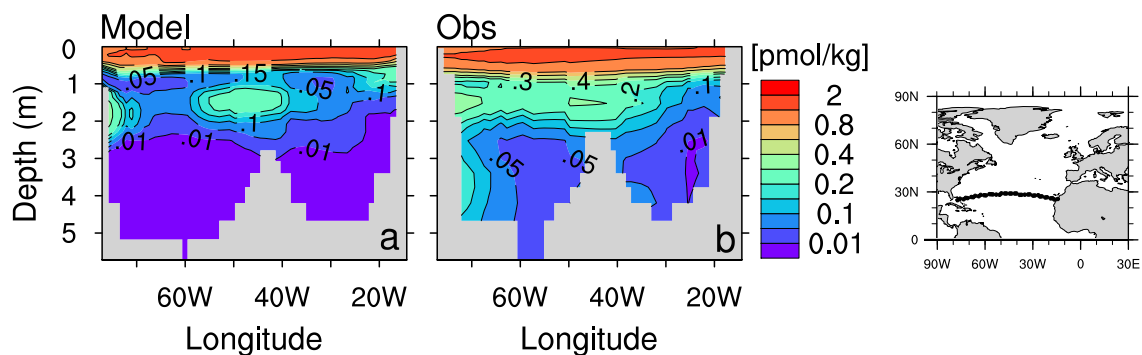
**Figure D3.** CFC-12 concentration (pmol kg $^{-1}$) in Feburary 1998 along the A5 section in the Atlantic Ocean (see right panel) of the model (a) and of observations from GLODAPv1 database (panel b; Key et al., 2004). Contour intervals are 0.01, 0.05, 0.1, 0.15, 0.2, 0.3, 0.4, 0.6, 0.8, 1.2 and 2 pmol kg $^{-1}$.
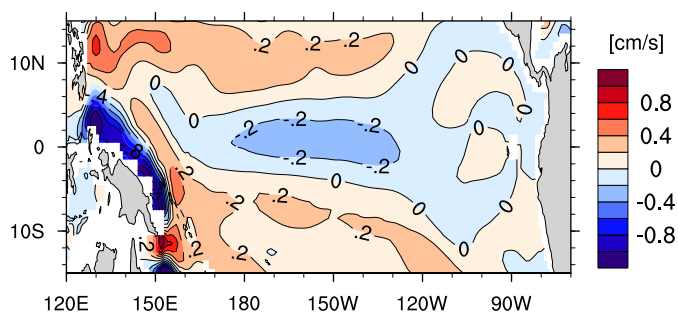
**Figure D4.** January 2003 - August 2009 mean zonal current (cm s $^{-1}$) at 960 m depth in the equatorial Pacific in the model. Positive values indicate eastward flow.

**Table D1.** Water masses and their definitions in the model

| water mass | definition in the model |
|---|---|
| Indian Ocean ventilated waters | |
| upwelling regions | north of $10°$N in the Arabian Sea; north of $8°$N in the Bay of Bengal |
| STGW (Subtropical Gyre Water), SAMW (Sub-Antarctic Mode Water) * | $\sigma_\theta \leq 27.0$ |
| AAIW (Antarctic Intermediate Water) | $27.0 < \sigma_\theta \leq 27.45$** |
| IDW (Indian Deep Water), CDW (Circumpolar Deep Water) | $\sigma_\theta > 27.45$** |
| North Pacific ventilated waters | |
| upwelling regions | east of $160°$W, south of $25°$N, $\sigma_\theta > 26.4$ |
| STGW | $\sigma_\theta \leq 26.7$ |
| NPIW (North Pacific Intermediate Water) | $\sigma_\theta > 26.7$ |
| South Pacific ventilated waters | |
| upwelling regions | east of $160°$W, north of $15°$S, $\sigma_\theta > 26.5$; east of $90°$W, north of $40°$N, $\sigma_\theta > 26.5$ |
| STGW, SAMW * | $\sigma_\theta \leq 27.15$ |
| AAIW | $26.7 < \sigma_\theta \leq 27.7$, salnity$< 35.0$ psu |
| PDW (Pacific Deep Water), CDW | $\sigma_\theta > 27.7$ |
| North Atlantic ventilated waters | |
| STGW | $\sigma_\theta \leq 27.2$, south of $45°$N |
| SPMW (Subpolar Mode Water) | $26.95 < \sigma_\theta \leq 27.5$** |
| NSOW (Nordic Seas Overflow Water), NADW (North Atlantic Deep Water), LSW (Labrador Sea Water) | $\sigma_\theta > 27.5$** |
| South Atlantic ventilated waters | |
| STGW | $\sigma_\theta \leq 26.9$ |
| SAMW, AAIW * | $26.9 < \sigma_\theta < 27.4$ |
| AABW (Antarctic Bottom Water), CDW | $\sigma_\theta > 27.4$ |

* Water masses are combined together rather than separately defined as in Eide et al. (2017a).

** A different $\sigma_\theta$ threshold is used here compared to Eide et al. (2017a).
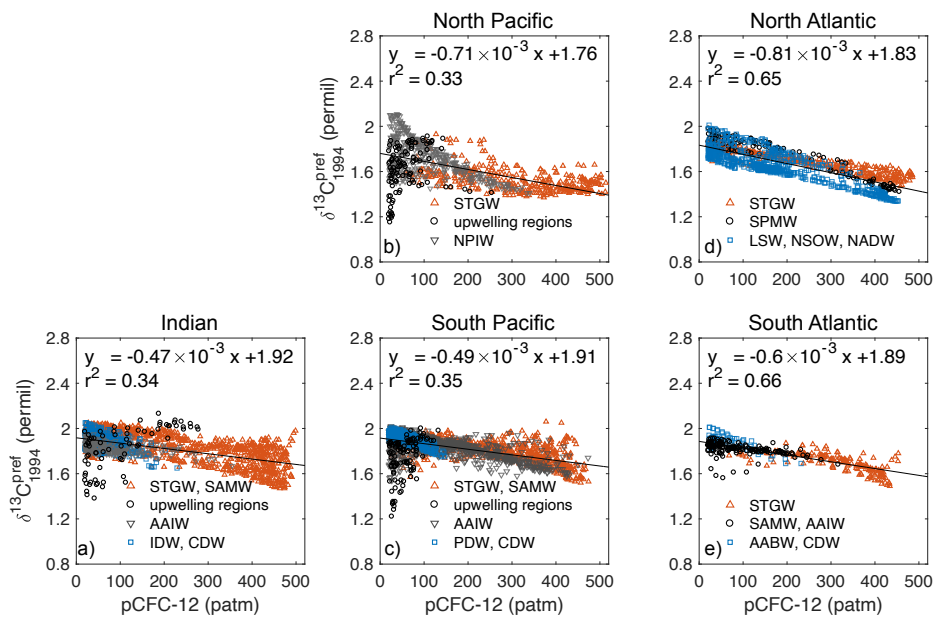
**Figure D5.** Regressional relationships between pCFC-12$_{1994}$ and $\delta^{13}C^{pref}_{1994}$ for the Indian Ocean (a), the North Pacific (b), the South Pacific (c), the North Atlantic (d) and the South Atlantic (e). Different colours and symbols indicates different water masses. The full names, as well as the definitions, of the water masses are listed in Table D1.
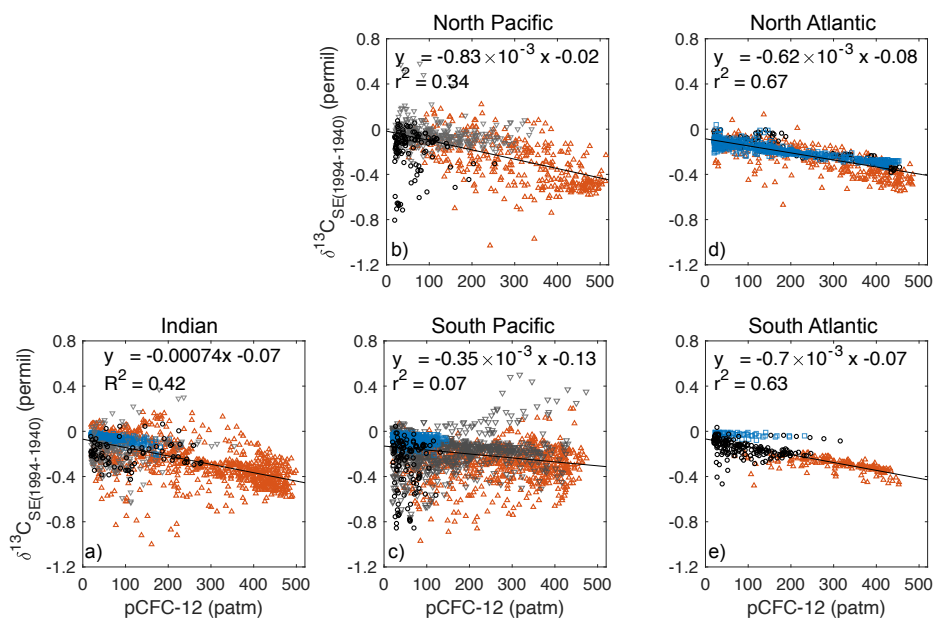
**Figure D6.** As Fig. D5, but for the relationships between pCFC-12$_{1994}$ and $\delta^{13}C_{SE(1994-1940)}$.
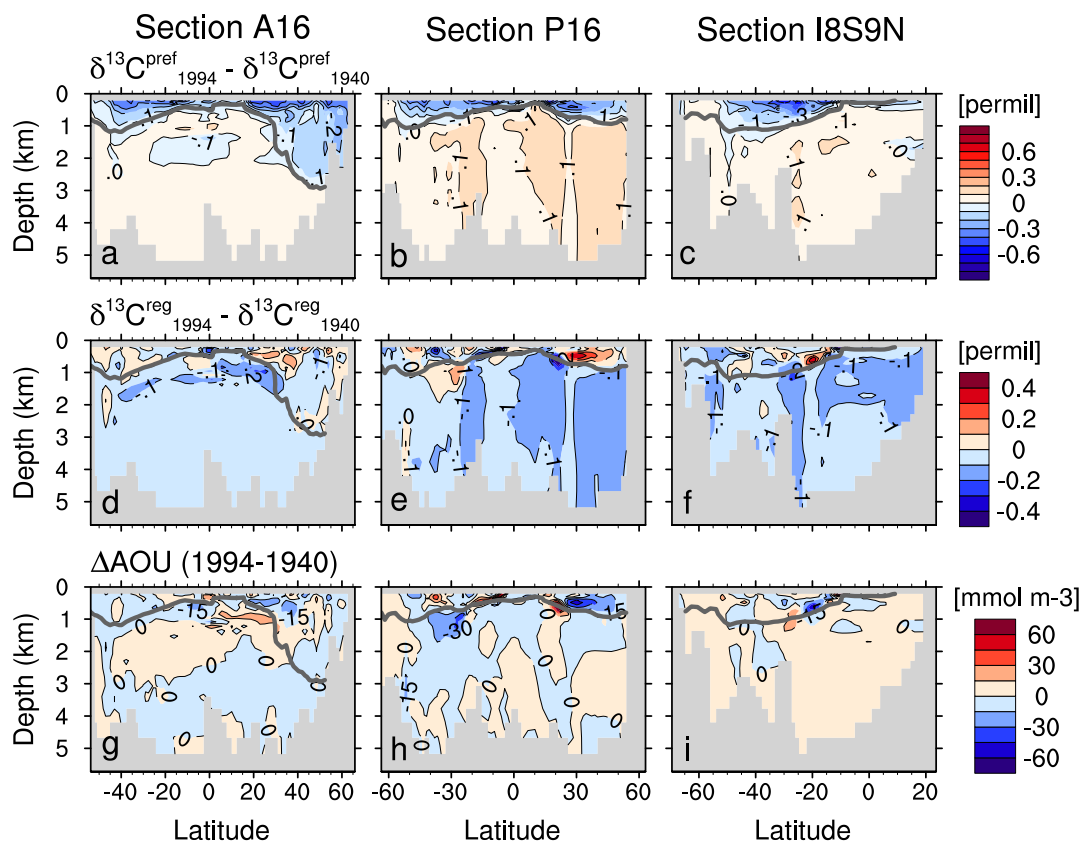
**Figure D7.** The change of the preformed component of $\delta^{13}C_{DIC}$ (‰) between 1994 and 1940 at sections A16 (a), P16 (b) and I8S9N (c). The thick grey line is pCFC-12$_{1994}$ = 20 isoline. (d - f) and (g - i): as (a - c), but for the change in the regenerated component of $\delta^{13}C_{DIC}$ (‰) and the change of AOU (mmol m$^{-3}$), respectively.
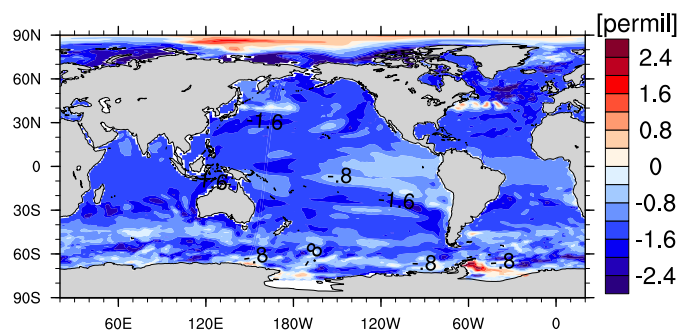
**Figure D8.** The change of surface $\delta^{13}C_{POC}$ (‰) between 1994 and 1940.
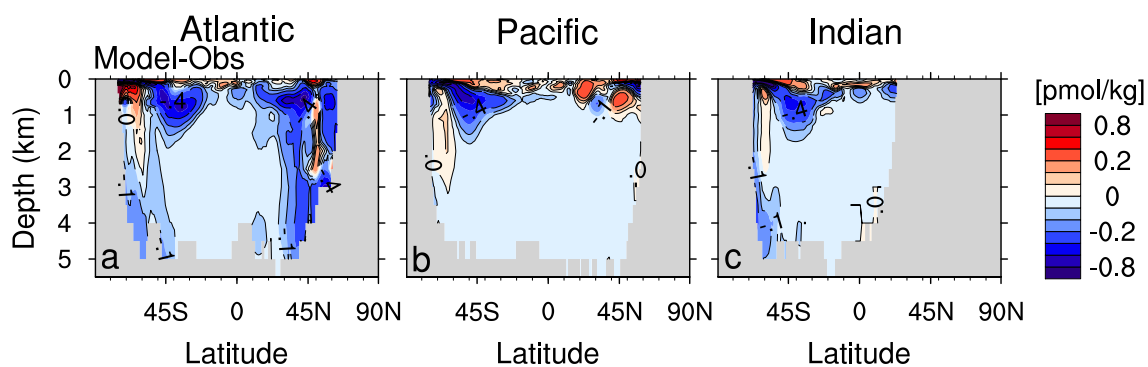
**Figure D9.** The difference of zonal-mean CFC-12 concentration (pmol kg$^{-1}$) between model and observations from GLODAPv1 database (Key et al., 2004) for the Atlantic (a) the Pacific (b) and the Indian Ocean (c). Modal data is averaged for the period 1990s. Negative values indicate lower CFC-12 concentration in the model than observation. The isolines are 0, ±0.05, ±0.1, ±0.2, ±0.4, ±0.6, ±0.8 pmol/kg.

*Code and data availability.* Primary data and code for this study are available from the corresponding author upon request. All observational data used in this study are available from public databases or literature, which can be found in the corresponding references.

*Author contributions.* BL performed the $^{13}$C model development, conducted the simulations and wrote the manuscript. KDS contributed in model implementation and setting up the experiments. All authors of the paper critically discussed the analysis of the results and provided
655   valuable input on the presentation of the manuscript.

*Competing interests.* The authors declare that they have no conflict of interest.

*Acknowledgements.* This research was supported by the German palaeoclimate modelling initiative PalMod (FKZ: 01LP1505A, 01LP1515C). PalMod is part of the Research for Sustainable Development initiative (FONA) funded by the German Federal Ministry of Education and Research (BMBF). Simulations were performed at the German Climate Computing Center (DKRZ). We thank Dr. Irene Stemmler for her
660   valuable input and we thank Dr. Friederike Fröb for internal review of this manuscript.

## References

Aumont, O., Orr, J. C., Monfray, P., Madec, G., and Maier-Reimer, E.: Nutrient trapping in the equatorial Pacific: The ocean circulation solution, Global Biogeochemical Cycles, 13, 351–369, https://doi.org/10.1029/1998GB900012, 1999.

Bacastow, R. B., Keeling, C. D., Lueker, T. J., Wahlen, M., and Mook, W. G.: The $^{13}$C Suess Effect in the world surface oceans
665    and its implications for oceanic uptake of CO2: Analysis of observations at Bermuda, Global Biogeochemical Cycles, 10, 335–346, https://doi.org/10.1029/96GB00192, 1996.

Böhm, F., Joachimski, M., Lehnert, H., Morgenroth, G., Kretschmer, W., Vacelet, J., and Dullo, W.-C.: Carbon isotope records from extant Caribbean and South Pacific sponges: Evolution of $\delta^{13}$C in surface water DIC, Earth and Planetary Science Letters, 139, 291–303, https://doi.org/10.1016/0012-821X(96)00006-4, 1996.

670    Böhm, F., Joachimski, M. M., Dullo, W.-C., Eisenhauer, A., Lehnert, H., Reitner, J., and Wörheide, G.: Oxygen isotope fractionation in marine aragonite of coralline sponges, Geochimica et Cosmochimica Acta, 64, 1695–1703, https://doi.org/10.1016/S0016-7037(99)00408-1, 2000.

Boyd, P. W., Watson, A. J., Law, C. S., Abraham, E. R., Trull, T., Murdoch, R., Bakker, D. C. E., Bowie, A. R., Buesseler, K. O., Chang, H., Charette, M., Croot, P., Downing, K., Frew, R., Gall, M., Hadfield, M., Hall, J., Harvey, M., Jameson, G., LaRoche, J., Liddicoat, M., Ling,
675    R., Maldonado, M. T., McKay, R. M., Nodder, S., Pickmere, S., Pridmore, R., Rintoul, S., Safi, K., Sutton, P., Strzepek, R., Tanneberger, K., Turner, S., Waite, A., and Zeldis, J.: A mesoscale phytoplankton bloom in the polar Southern Ocean stimulated by iron fertilization, Nature, 407, 695–702, https://doi.org/10.1038/35037500, 2000.

Broecker, W. S. and Maier-Reimer, E.: The influence of air and sea exchange on the carbon isotope distribution in the sea, Global Biogeochemical Cycles, 6, 315–320, https://doi.org/10.1029/92GB01672, 1992.

680    Broecker, W. S. and Peng, T. H.: Gas exchange rates between air and sea, Tellus, 26, 21–35, https://doi.org/10.3402/tellusa.v26i1-2.9733, 1974.

Broecker, W. S. and Peng, T. H.: Evaluation of the $^{13}$C constraint on the uptake of fossil fuel CO2 by the ocean, Global Biogeochemical Cycles, 7, 619–626, https://doi.org/10.1029/93GB01445, 1993.

Bullister, J. L.: Atmospheric Histories (1765-2015) for CFC-11, CFC-12, CFC-113, CCl4, SF6 and N2O (NCEI Accession 0164584), NOAA
685    National Centers for Environmental Information, https://doi.org/10.3334/CDIAC/otg.CFC_ATM_Hist_2015, 2017.

Chavez, F. P., Buck, K. R., Service, S. K., Newton, J., and Barber, R. T.: Phytoplankton variability in the central and eastern tropical Pacific, Deep Sea Research Part II: Topical Studies in Oceanography, 43, 835–870, https://doi.org/10.1016/0967-0645(96)00028-8, 1996.

Craig, H.: Isotopic standards for carbon and oxygen and correction factors for mass-spectrometric analysis of carbon dioxide, Geochimica et Cosmochimica Acta, 12, 133–149, https://doi.org/10.1016/0016-7037(57)90024-8, 1957.

690    Cravatte, S., Kessler, W. S., and Marin, F.: Intermediate Zonal Jets in the Tropical Pacific Ocean Observed by Argo Floats*, Journal of Physical Oceanography, 42, 1475–1485, https://doi.org/10.1175/JPO-D-11-0206.1, 2012.

Curry, W. B. and Oppo, D. W.: Glacial water mass geometry and the distribution of $\delta^{13}$C of $\Sigma CO_2$ in the western Atlantic Ocean, Paleoceanography, 20, PA1017, https://doi.org/10.1029/2004PA001021, 2005.

de Boyer Montégut, C., Madec, G., Fischer, A. S., Lazar, A., and Iudicone, D.: Mixed layer depth over the global ocean:
695    An examination of profile data and a profile-based climatology, Journal of Geophysical Research: Oceans, 109, C12 003, https://doi.org/10.1029/2004JC002378, 2004.

Degens, E., Behrendt, M., Gotthardt, B., and Reppmann, E.: Metabolic fractionation of carbon isotopes in marine plankton - II. Data on samples collected off the coasts of Peru and Ecuador, Deep Sea Research, 15, 11–20, https://doi.org/10.1016/0011-7471(68)90025-9, 1968.

700 Dentith, J. E., Ivanovic, R. F., Gregoire, L. J., Tindall, J. C., and Robinson, L. F.: Simulating stable carbon isotopes in the ocean component of the FAMOUS general circulation model with MOSES1 (XOAVI), Geoscientific Model Development, 13, 3529–3552, https://doi.org/10.5194/gmd-13-3529-2020, 2020.

Dietze, H. and Loeptien, U.: Revisiting 'nutrient trapping' in global coupled biogeochemical ocean circulation models, Global Biogeochemical Cycles, 27, 265–284, https://doi.org/10.1002/gbc.20029, 2013.

705 Dutay, J.-C., Bullister, J. L., Doney, S. C., Orr, J. C., Najjar, R., Caldeira, K., Campin, J.-M., Drange, H., Follows, M., Gao, Y., Gruber, N., Hecht, M. W., Ishida, A., Joos, F., Lindsay, K., Madec, G., Maier-Reimer, E., Marshall, J. C., Matear, R. J., Monfray, P., Mouchet, A., Plattner, G.-K., Sarmiento, J., Schlitzer, R., Slater, R., Totterdell, I. J., Weirig, M.-F., Yamanaka, Y., and Yool, A.: Evaluation of ocean model ventilation with CFC-11: comparison of 13 global ocean models, Ocean Modelling, 4, 89–120, https://doi.org/10.1016/S1463-5003(01)00013-0, 2002.

710 Eide, M., Olsen, A., Ninnemann, U. S., and Eldevik, T.: A global estimate of the full oceanic $^{13}$C Suess effect since the preindustrial, Global Biogeochemical Cycles, 31, 492–514, https://doi.org/10.1002/2016GB005472, 2017a.

Eide, M., Olsen, A., Ninnemann, U. S., and Johannessen, T.: A global ocean climatology of preindustrial and modern ocean $\delta^{13}$C, Global Biogeochemical Cycles, 31, 515–534, https://doi.org/10.1002/2016GB005473, 2017b.

Francois, R., Altabet, M. A., Goericke, R., McCorkle, D. C., Brunet, C., and Poisson, A.: Changes in the $\delta^{13}$C of surface water par-
715 ticulate organic matter across the subtropical convergence in the SW Indian Ocean, Global Biogeochemical Cycles, 7, 627–644, https://doi.org/10.1029/93GB01277, 1993.

Gammon, R. H., Cline, J., and Wisegarver, D.: Chlorofluoromethanes in the northeast Pacific Ocean: Measured vertical distributions and application as transient tracers of upper ocean mixing, Journal of Geophysical Research: Oceans, 87, 9441–9454, https://doi.org/10.1029/JC087iC12p09441, 1982.

720 Garcia, H. E., Locarnini, R. A., Boyer, T. P., Antonov, J. I., Baranova, O. K., Zweng, M. M., Reagan, J. R., and Johnson, D. R.: World Ocean Atlas 2013, Volume 4: Dissolved Inorganic Nutrients (phosphate, nitrate, silicate), Tech. Rep. 25, NOAA Atlas NESDIS 76, 2013a.

Garcia, H. E., Locarnini, R. A., Boyer, T. P., Antonov, J. I., Baranova, O. K., Zweng, M. M., Reagan, J. R., and Johnson, D. R.: World Ocean Atlas 2013, Volume 3: Dissolved Oxygen, Apparent Oxygen Utilization, and Oxygen Saturation, Tech. Rep. 27, NOAA Atlas NESDIS 75, 2013b.

725 Goericke, R. and Fry, B.: Variations of marine plankton $\delta^{13}$C with latitude, lemperature, and dissolved $CO_2$ in the world Ocean, Global Biogeochemical Cycles, 8, 85–90, https://doi.org/10.1029/93gb03272, 1994.

Gruber, N., Keeling, C. D., Bacastow, R. B., Guenther, P. R., Lueker, T. J., Wahlen, M., Meijer, H. A. J., Mook, W. G., and Stocker, T. F.: Spatiotemporal patterns of carbon-13 in the global surface oceans and the oceanic Suess effect, Global Biogeochemical Cycles, 13, 307–335, https://doi.org/10.1029/1999GB900019, 1999.

730 Hansman, R. L. and Sessions, A. L.: Measuring the in situ carbon isotopic composition of distinct marine plankton populations sorted by flow cytometry, Limnology and Oceanography: Methods, 14, 87–99, https://doi.org/10.1002/lom3.10073, 2016.

Heinze, C., Maier-Reimer, E., Winguth, A. M. E., and Archer, D.: A global oceanic sediment model for long-term climate studies, Global Biogeochemical Cycles, 13, 221–250, https://doi.org/10.1029/98GB02812, 1999.

Hofmann, M., Wolf-Gladrow, D. A., Takahashi, T., Sutherland, S. C., Six, K. D., and Maier-Reimer, E.: Stable carbon isotope distribution of
735    particulate organic matter in the ocean: a model study, Marine Chemistry, 72, 131–150, https://doi.org/10.1016/S0304-4203(00)00078-5,
       2000.

Holte, J., Talley, L. D., Gilson, J., and Roemmich, D.: An Argo mixed layer climatology and database, Geophysical Research Letters, 44,
       5618–5626, https://doi.org/10.1002/2017GL073426, 2017.

Ilyina, T., Six, K. D., Segschneider, J., Maier-Reimer, E., Li, H., and Núñez-Riboni, I.: Global ocean biogeochemistry model HAMOCC:
740    Model architecture and performance as component of the MPI-Earth system model in different CMIP5 experimental realizations, Journal
       of Advances in Modeling Earth Systems, 5, 287–315, https://doi.org/10.1029/2012MS000178, 2013.

Jahn, A., Lindsay, K., Giraud, X., Gruber, N., Otto-Bliesner, B. L., Liu, Z., and Brady, E. C.: Carbon isotopes in the ocean model of the
       Community Earth System Model (CESM1), Geoscientific Model Development, 8, 2419–2434, https://doi.org/10.5194/gmd-8-2419-2015,
       2015.

745 Jones, C. D., Arora, V., Friedlingstein, P., Bopp, L., Brovkin, V., Dunne, J., Graven, H., Hoffman, F., Ilyina, T., John, J. G., Jung,
       M., Kawamiya, M., Koven, C., Pongratz, J., Raddatz, T., Randerson, J. T., and Zaehle, S.: C4MIP – The Coupled Climate–
       Carbon Cycle Model Intercomparison Project: experimental protocol for CMIP6, Geoscientific Model Development, 9, 2853–2880,
       https://doi.org/10.5194/gmd-9-2853-2016, 2016.

Jungclaus, J. H., Fischer, N., Haak, H., Lohmann, K., Marotzke, J., Matei, D., Mikolajewicz, U., Notz, D., and Storch, J. S.: Characteristics of
750    the ocean simulations in the Max Planck Institute Ocean Model (MPIOM) the ocean component of the MPI-Earth system model, Journal
       of Advances in Modeling Earth Systems, 5, 422–446, https://doi.org/10.1002/jame.20023, 2013.

Keeling, C. D.: The Suess effect: $^{13}$Carbon-$^{14}$Carbon interrelations, Environment International, 2, 229–300, https://doi.org/10.1016/0160-
       4120(79)90005-9, 1979.

Keller, K. and Morel, F. M. M.: A model of carbon isotopic fractionation and active carbon uptake in phytoplankton, Marine Ecology Progress
755    Series, 182, 295–298, http://www.jstor.org/stable/24852139, 1999.

Key, R. M., Kozyr, A., Sabine, C. L., Lee, K., Wanninkhof, R., Bullister, J. L., Feely, R. A., Millero, F. J., Mordy, C., and Peng, T.-H.: A
       global ocean carbon climatology: Results from Global Data Analysis Project (GLODAP), Global Biogeochemical Cycles, 18, GB4031,
       https://doi.org/doi:10.1029/2004GB002247, 2004.

Landschützer, P., Gruber, N., and Bakker, D.: A 30 years observation-based global monthly gridded sea surface pCO$_2$ product
760    from 1982 through 2011, https://doi.org/10.3334/CDIAC/OTG.SPCO2_1982_2011_ETH_SOM-FFN, http://cdiac.ornl.gov/ftp/oceans/
       SPCO2_1982_2011_ETH_SOM_FFN, Carbon Dioxide Information Analysis Center, Oak Ridge National Laboratory, US Department
       of Energy, Oak Ridge, Tennessee, 2015.

Latif, M., Claussen, M., Schulz, M., and Brücher, T.: Comprehensive Earth system models of the last glacial cycle, Eos: Earth & Space
       Science News, 97, 2016.

765 Laws, E. A., Popp, B. N., Bidigare, R. R., Kennicutt, M. C., and Macko, S. A.: Dependence of phytoplankton carbon isotopic composition
       on growth rate and [CO$_2$]aq: Theoretical considerations and experimental results, Geochimica et Cosmochimica Acta, 59, 1131–1138,
       https://doi.org/10.1016/0016-7037(95)00030-4, 1995.

Letelier, R., Dore, J., Winn, C., and Karl, D.: Seasonal and interannual variations in photosynthetic carbon assimilation at Station, Deep Sea
       Research Part II: Topical Studies in Oceanography, 43, 467–490, https://doi.org/10.1016/0967-0645(96)00006-9, 1996.

770 Liang, X., Spall, M., and Wunsch, C.: Global Ocean Vertical Velocity From a Dynamically Consistent Ocean State Estimate, Journal of
       Geophysical Research: Oceans, 122, 8208–8224, https://doi.org/10.1002/2017JC012985, 2017.

Lide, D. R.: CRC Handbook of Chemistry and Physics, CRC Press, Boca Raton, Florida, 2002.

Lynch-Stieglitz, J., Stocker, T. F., Broecker, W. S., and Fairbanks, R. G.: The influence of air-sea exchange on the isotopic composition of oceanic carbon: observations and modelling., Global Biogeochemical Cycles, 9, 653–665, https://doi.org/10.1029/95GB02574, 1995.

775   Maier-Reimer, E.: Geochemical cycles in an ocean general circulation model. Preindustrial tracer distributions, Global Biogeochemical Cycles, 7, 645–677, https://doi.org/10.1029/93GB01355, 1993.

Marañón, E.: Phytoplankton growth rates in the Atlantic subtropical gyres, Limnology and Oceanography, 50, 299–310, https://doi.org/10.4319/lo.2005.50.1.0299, 2005.

Martin, J. H., Knauer, G. A., Karl, D. M., and Broenkow, W. W.: VERTEX: carbon cycling in the northeast Pacific, Deep Sea Research Part
780   A. Oceanographic Research Papers, 34, 267–285, https://doi.org/10.1016/0198-0149(87)90086-0, 1987.

Mauritsen, T., Bader, J., Becker, T., Behrens, J., Bittner, M., Brokopf, R., and et al.: Developments in the MPI-M Earth System Model version 1.2 (MPI-ESM1.2) and Its Response to Increasing CO2, Journal of Advances in Modeling Earth System, 11, 998–1038, https://doi.org/10.1029/ 2018MS001400, 2019.

Meinshausen, M., Vogel, E., Nauels, A., Lorbacher, K., Meinshausen, N., Etheridge, D. M., Fraser, P. J., Montzka, S. A., Rayner, P. J.,
785   Trudinger, C. M., Krummel, P. B., Beyerle, U., Canadell, J. G., Daniel, J. S., Enting, I. G., Law, R. M., Lunder, C. R., O'Doherty, S., Prinn, R. G., Reimann, S., Rubino, M., Velders, G. J. M., Vollmer, M. K., Wang, R. H. J., and Weiss, R.: Historical greenhouse gas concentrations for climate modelling (CMIP6), Geoscientific Model Development, 10, 2057–2116, https://doi.org/10.5194/gmd-10-2057-2017, 2017.

Moore, C. M., Mills, M. M., Arrigo, K. R., Berman-Frank, I., Bopp, L., Boyd, P. W., Galbraith, E. D., Geider, R. J., Guieu, C., Jaccard, S. L.,
790   Jickells, T. D., La Roche, J., Lenton, T. M., Mahowald, N. M., Marañón, E., Marinov, I., Moore, J. K., Nakatsuka, T., Oschlies, A., Saito, M. A., Thingstad, T. F., Tsuda, A., and Ulloa, O.: Processes and patterns of oceanic nutrient limitation, Nature Geoscience, 6, 701–710, https://doi.org/10.1038/ngeo1765, 2013.

Msadek, R., Johns, W. E., Yeager, S. G., Danabasoglu, G., Del-worth, T. L., and Rosati, A.: The Atlantic meridional heat transport at 26.5 N and its relationship with the MOC in the RAPID array and the GFDL and NCAR coupled models, Journal of Climate, 26, 4335–4356,
795   https://doi.org/10.1175/JCLI-D-12-00081.1, 2013.

Notz, D., Haumann, F. A., Haak, H., Jungclaus, J. H., , and Marotzke, J.: Arctic sea-ice evolution as modeled by Max Planck Institute for Meteorology's Earth system model, Journal of Advances in Modeling Earth Systems, 5, 173–194, https://doi.org/10.1002/jame.20016, 2013.

O'Leary, M. H.: Carbon Isotopes in Photosynthesis, BioScience, 38, 328–336, https://doi.org/10.2307/1310735, 1988.

800   Olsen, A. and Ninnemann, U.: Large $\delta^{13}$C Gradients in the Preindustrial North Atlantic Revealed, Science, 330, 658–659, https://doi.org/10.1126/science.1193769, 2010.

Olsen, A., Key, R. M., van Heuven, S., Lauvset, S. K., Velo, A., Lin, X., Schirnick, C., Kozyr, A., Tanhua, T., Hoppema, M., Jutterström, S., Steinfeldt, R., Jeansson, E., Ishii, M., Pérez, F. F., and Suzuki, T.: The Global Ocean Data Analysis Project version 2 (GLODAPv2) – an internally consistent data product for the world ocean, Earth System Science Data, 8, 297–323, https://doi.org/10.5194/essd-8-297-2016,
805   2016.

O'Neill, C. M., Hogg, A. M., Ellwood, M. J., Eggins, S. M., and Opdyke, B. N.: The [simple carbon project] model v1.0, Geoscientific Model Development, 12, 1541–1572, https://doi.org/10.5194/gmd-12-1541-2019, 2019.

Orr, J. C., Najjar, R. G., Aumont, O., Bopp, L., Bullister, J. L., Danabasoglu, G., Doney, S. C., Dunne, J. P., Dutay, J.-C., Graven, H., Griffies, S. M., John, J. G., Joos, F., Levin, I., Lindsay, K., Matear, R. J., McKinley, G. A., Mouchet, A., Oschlies, A., Romanou, A., Schlitzer, R.,

810   Tagliabue, A., Tanhua, T., and Yool, A.: Biogeochemical protocols and diagnostics for the CMIP6 Ocean Model Intercomparison Project (OMIP), Geoscientific Model Development, 10, 2169–2199, https://doi.org/10.5194/gmd-10-2169-2017, 2017.

Paulsen, H., Ilyina, T., Six, K. D., and Stemmler, I.: Incorporating a prognostic representation of marine nitrogen fixers into the global ocean biogeochemical model HAMOCC, Journal of Advances in Modeling Earth Systems, 9, 438–464, https://doi.org/10.1002/2016MS000737, 2017.

815   Peterson, C. D., Lisiecki, L. E., and Stern, J. V.: Deglacial whole-ocean $\delta^{13}$C change estimated from 480 benthic foraminiferal records, Paleoceanography, 29, 549–563, https://doi.org/10.1002/2013PA002552, 2014.

Poli, P., Hersbach, H., Dee, D. P., Berrisford, P., Simmons, A. J., Vitart, F., Laloyaux, P., Tan, D. G. H., Peubey, C., Thépaut, J.-N., Trémolet, Y., Hólm, E. V., Bonavita, M., Isaksen, L., and Fisher, M.: ERA-20C: An Atmospheric Reanalysis of the Twentieth Century, Journal of Climate, 29, 4083–4097, https://doi.org/10.1175/JCLI-D-15-0556.1, 2016.

820   Popp, B. N., Takigiku, R., Hayes, J. M., Louda, J. W., and Baker, E. W.: The post-Paleozoic chronology and mechanism of $^{13}$C depletion in primary marine organic matter, American Journal of Science, 289, 436–454, https://doi.org/10.2475/ajs.289.4.436, 1989.

Popp, B. N., Laws, E. A., Bidigare, R. R., Dore, J. E., Hanson, K. L., and Wakeham, S. G.: Effect of Phytoplankton Cell Geometry on Carbon Isotopic Fractionation, Geochimica et Cosmochimica Acta, 62, 69–77, https://doi.org/10.1016/S0016-7037(97)00333-5, 1998.

Quay, P., Sonnerup, R., Westby, T., Stutsman, J., and McNichol, A.: Changes in the $^{13}$C/$^{12}$C of dissolved inorganic carbon in the ocean as a
825   tracer of anthropogenic CO$_2$ uptake, Global Biogeochemical Cycles, 17(1), 1004, https://doi.org/10.1029/2001GB001817, 2003.

Rau, G. H., Riebesell, U., and Wolf-Gladrow, D.: A model of photosynthetic $^{13}$C fractionation by marine phytoplankton based on diffusive molecular CO$_2$ uptake, Marine Ecology Progress Series, 133, 275–285, https://doi.org/10.3354/meps133275, 1996.

Sabine, C. L., Feely, R. A., Gruber, N., Key, R. M., Lee, K., Bullister, J. L., Wanninkhof, R., Wong, C. S., Wallace, D. W. R., Tilbrook, B., Millero, F. J., Peng, T.-H., Kozyr, A., Ono, T., and Rios, A. F.: The Oceanic Sink for Anthropogenic CO$_2$, Science, 305, 367–371,
830   https://doi.org/10.1126/science.1097403, 2004.

Schmittner, A., Gruber, N., Mix, A. C., Key, R. M., Tagliabue, A., and Westberry, T. K.: Biology and air-sea gas exchange controls on the distribution of carbon isotope ratios ($\delta^{13}$C) in the ocean, Biogeosciences, 10, 5793–5816, https://doi.org/10.5194/bg-10-5793-2013, 2013.

Schmittner, A., Bostock, H. C., Cartapanis, O., Curry, W. B., Filipsson, H. L., Galbraith, E. D., Gottschalk, J., Herguera, J. C., Hoogakker, B., Jaccard, S. L., Lisiecki, L. E., Lund, D. C., Martínez-Méndez, G., Lynch-Stieglitz, J., Mackensen, A., Michel, E., Mix, A. C., Oppo,
835   D. W., Peterson, C. D., Repschläger, J., Sikes, E. L., Spero, H. J., and Waelbroeck, C.: Calibration of the carbon isotope composition ($\delta^{13}$C) of benthic foraminifera, Paleoceanography, 32, 512–530, https://doi.org/10.1002/2016PA003072, 2017.

Silsbe, G. M., Behrenfeld, M. J., Halsey, K. H., Milligan, A. J., and Westberry, T. K.: The CAFE model: A net production model for global ocean phytoplankton, Global Biogeochemical Cycles, 30, 1756–1777, https://doi.org/10.1002/2016GB005521, 2016.

Six, K. D. and Maier-Reimer, E.: Effects of plankton dynamics on seasonal carbon fluxes in an ocean general circulation model, Global
840   Biogeochemical Cycles, 10, 559–583, https://doi.org/10.1029/96GB02561, 1996.

Smeed, D., McCarthy, G., Rayner, D., Moat, B. I., Johns, W. E., Baringer, M. O., and Meinen, C. S.: Atlantic meridional overturning circulation observed by the RAPID-MOCHA-WBTS (RAPID-Meridional Overturning Circulation and Heatflux Array-Western Boundary Time Series) array at 26N from 2004 to 2017., British Oceanographic Data Centre, Natural Environment Research Council, https://doi.org/10.5285/5acfd143-1104-7b58-e053-6c86abc0d94b, 2017.

845   Sonnerup, R. E., Quay, P. D., McNichol, A. P., Bullister, J. L., Westby, T. A., and Anderson, H. L.: Reconstructing the oceanic $^{13}$C Suess Effect, Global Biogeochemical Cycles, 13, 857–872, https://doi.org/10.1029/1999GB900027, 1999.

Sonnerup, R. E., Mcnichol, A. P., Quay, P. D., Gammon, R. H., Bullister, J. L., Sabine, C. L., and Slater, R. D.: Anthropogenic $\delta^{13}$C changes in the North Pacific Ocean reconstructed using a multiparameter mixing approach (MIX), Tellus B: Chemical and Physical Meteorology, 59, 303–317, https://doi.org/10.1111/j.1600-0889.2007.00250.x, 2007.

850 Swart, P. K., Thorrold, S., Rosenheim, B., Eisenhauer, A., Harrison, C. G. A., Grammer, M., and Latkoczy, C.: Intra-annual variation in the stable oxygen and carbon and trace element composition of sclerosponges, Paleoceanography, 17, 1045, https://doi.org/10.1029/2000PA000622, 2002.

Swart, P. K., Greer, L., Rosenheim, B. E., Moses, C. S., Waite, A. J., Winter, A., Dodge, R. E., and Helmle, K.: The $^{13}$C Suess effect in scleractinian corals mirror changes in the anthropogenic $CO_2$ inventory of the surface oceans, Geophysical Research Letters, 37, L05 604,
855 https://doi.org/10.1029/2009GL041397, 2010.

Tagliabue, A. and Bopp, L.: Towards understanding global variability in ocean carbon-13, Global Biogeochemical Cycles, 22, GB1025, https://doi.org/10.1029/2007GB003037, 2008.

Takahashi, T., Broecker, W. S., and Langer, S.: Redfield ratio based on chemical data from isopycnal surfaces, Journal of Geophysical Research: Oceans, 90, 6907–6924, https://doi.org/10.1029/JC090iC04p06907, 1985.

860 Takahashi, T., Sutherland, S., Chipman, D., Goddard, J., Ho, C., Newberger, T., Sweeney, C., and Munro, D.: Climatological distributions of pH, pCO2, total CO2, alkalinity, and CaCO3 saturation in the global surface ocean, and temporal changes at selected locations, Marine Chemistry, 164, 95–125, https://doi.org/10.1016/j.marchem.2014.06.004, 2014.

Tjiputra, J. F., Schwinger, J., Bentsen, M., Morée, A. L., Gao, S., Bethke, I., Heinze, C., Goris, N., Gupta, A., He, Y., Olivié, D., Seland, Ø., and Schulz, M.: Ocean biogeochemistry in the Norwegian Earth System Model version 2 (NorESM2), Geoscientific Model Development,
865 2020, 1–64, https://doi.org/10.5194/gmd-13-2393-2020, 2020.

Tuerena, R. E., Ganeshram, R. S., Humphreys, M. P., Browning, T. J., Bouman, H., and Piotrowski, A. P.: Isotopic fractionation of carbon during uptake by phytoplankton across the South Atlantic subtropical convergence, Biogeosciences Discussions, 2019, 1–29, https://doi.org/10.5194/bg-2019-162, 2019.

Turner, J. V.: Kinetic fractionation of carbon-13 during calcium carbonate precipitation, Geochimica et Cosmochimica Acta, 46, 1183–1191,
870 https://doi.org/10.1016/0016-7037(82)90004-7, 1982.

Wanninkhof, R.: Relationship between wind speed and gas exchange over the ocean revisited, Limnology and Oceanography: Methods, 12, 351–362, https://doi.org/10.4319/lom.2014.12.351, 2014.

Weisberg, R. H. and Qiao, L.: Equatorial Upwelling in the Central Pacific Estimated from Moored Velocity Profilers, Journal of Physical Oceanography, 30, 105–124, https://doi.org/10.1175/1520-0485(2000)030<0105:EUITCP>2.0.CO;2, 2000.

875 Weiss, R. F.: Carbon dioxide in water and seawater: the solubility of a non-ideal gas, Marine Chemistry, 2, 203–215, https://doi.org/10.1016/0304-4203(74)90015-2, 1974.

Westberry, T., Behrenfeld, M. J., Siegel, D. A., and Boss, E.: Carbon-based primary productivity modeling with vertically resolved photoac-climation, Global Biogeochemical Cycles, 22, GB2024, https://doi.org/10.1029/2007GB003078, 2008.

Wörheide, G.: The reef cave dwelling ultraconservative coralline demospongeAstrosclera willeyanaLister 1900 from the Indo-Pacific, Facies,
880 38, 1–88, https://doi.org/10.1007/BF02537358, 1998.

Zeeb, R. E. and Wolf-Gladrow, D. A.: CO2 in Seawater: Equilibrium, Kinetics, Isotopes, Elsevier Oceanography Series, Amsterdam, 2001.

Zhang, J., Quay, P., and Wilbur, D.: Carbon isotope fractionation during gas-water exchange and dissolution of $CO_2$, Geochimica et Cosmochimica Acta, 59, 107–114, https://doi.org/10.1016/0016-7037(95)91550-D, 1995.